Computers and Structures 273 (2022) 106894

Contents lists available at ScienceDirect

Computers and Structures

journal homepage: www.elsevier.com/locate/compstruc

An analysis of embedded weak discontinuity approaches for the finite element modelling of heterogeneous materials

A. Ortega, E. Roubin, Y. Malecot, L. Daudeville

Univ. Grenoble Alpes, CNRS, Grenoble INP, 3SR, F-38000 Grenoble, France

ARTICLE INFO

Article history:
Received 4 April 2022
Accepted 24 August 2022

Keywords:
E-FEM modelling
Embedded weak discontinuity
Enhanced finite elements
Incompatible modes
Local heterogeneity modelling
Finite element enhancement functions

ABSTRACT

This paper analyses in detail the use of the Embedded Finite Element Method (E-FEM) to simulate local material heterogeneities. The work starts by a short review on the evolution of weak discontinuity models within the E-FEM framework to discuss how they account for the presence of multiple materials within a single element structure. A theoretical basis is introduced through some mathematical weak discontinuity definitions and the Hu-Washizu variational principle, for then establishing a set of requirements for retaining variational and kinematic consistency for any weak discontinuity enhancement proposal. From a general definition of a displacement enhancement field, two particular enhancement functions are derived by considering different consistency requirements: one which has been typically used in previous works and other which truly possesses variational consistency. A discussion is held on enhancement stability properties and the impact to global finite element solution processes. In the end, numerical simulations are made to assess the performance of each of these enhancements on the task of modelling a classical bi-material layered 3D tension problem and a more realistic heterogeneous sample having spherical inclusions of different radii. The final discussion evaluates both model performance and ease of implementation.

1. Introduction

The numerical modeling of the heterogeneous nature of some materials is important for studying and predicting complex features of their physical behavior, including their mechanical response and resistance under specific conditions.

Typical numerical analysis techniques such as the finite element or finite difference methods generally approach this problem considering homogeneous base domains. This requires a homogenisation procedure for a determined representative patch of the heterogeneous material. In order for this homogenised patch to be considered as truly representative, it should be large enough to exhibit the same mechanical properties of the material at large scales as in a whole continuum, but should also still remain small enough to be able to distinguish and explicitly model its heterogeneous structure. Such is the basis of representative volume element (RVE) approaches [1,2].

At some point, every approach following this line will require a realistic modeling of a limited domain in the scale in which the heterogeneities of a given material can be geometrically described in an accurate way. For such multi-scale simulation processes, a classical FEM approach will require an adapted mesh for the small scale to consistently capture the geometrical distribution of material heterogeneities in such domain. While sophisticated meshing adaptation techniques for heterogeneous objects are still an active subject of study [3,4], the approach remains computationally expensive and mathematically complicated, depending always on the arbitrary shapes of the different material phases present on the heterogeneous structure. This is specially true when a study requires the analysis of a large amount of heterogeneity distribution samples for a meaningful statistical treatment, such as in the execution of Monte Carlo methods that require repetitive sampling for the homogenisation process [5].

Alternative approaches for the numerical modelling of heterogeneous material domains have emerged, such as Voronoi cell techniques [6], discrete elements for granular rocks [7] or reinforced concrete [8], or the advanced finite element methods [9–11]. Some of these approaches will focus more on the material interfaces, like the Voronoi cells that make use of mixed 1-D finite elements to represent the presence of different material domains and the strength of the mechanical connection between them. Typically, it is the finite element methods in two or three dimensions that will grant a more meaningful representation of the state of stresses in continuous material models, since they attempt a more

https://doi.org/10.1016/j.compstruc.2022.106894
0045-7949/

direct and accurate geometrical description of material heterogeneities.

In regards to the latter, the *meshfree* or non-adaptive mesh approaches have been introduced as an attractive solution to this modelling problem. Applications of many advanced FEM techniques can be found, such as the Generalized Finite Element Method (G-FEM) [12–14], the Extended Finite Element Method (X-FEM) [15–17], the Base Force Element Method (B-FEM) [18,19] or the Embedded Finite Element Method (E-FEM) [20–22], the last one being precisely the scope of study in this work.

Although the specific modelling of 3D crack initiation and propagation events does not remain the principal scope of this work, the authors would also to remark that meshfree and non-adaptive mesh approaches have been actively used for recent advances on this subject, which remains by itself a center of interest for potential applications of the E-FEM framework with embedded discontinuities. From the side of meshfree approaches, we can account for the use of the local partition of unity (the cracking particle method) [23,24] or extended versions of the element-free Galerkin method [25]. On the other side, the X-FEM approach, which has recently benefited from improved conditioning on account of Cut Finite Element Methods [26], has been successfully applied for the study of non-planar crack prorogation problems and 3D linear elastic fracture analysis [27–31].

One of the most important intrinsic characteristics of the E-FEM framework is the lack of mechanical field continuity through different internal element domains, as its core foundation is based on the Principle of Incompatible Modes [32]. The approach retains a *local* definition for the mathematical enhancements used to represent material heterogeneities or internal element fractures. This implies that the effects of embedded discontinuities and their associated degrees of freedom can be resolved at elemental level without the need of incorporating global degrees of freedom to a given mechanical system. This is also remarked as the most prominent difference with respect to other advanced finite element methods such as the X-FEM, which uses a definition of the enhanced degrees of freedom directly reflected upon the nodal shape functions, with the need to resolve these enhanced degrees of freedom along with the remaining finite element assembly of the entire system. This is referred to as a *global approach* by the authors of this work, compared to an exclusively local setting where enhancements are entirely resolved at a local level. A detailed discussion highlighting this and other fundamental differences between the X-FEM and the E-FEM approach studied in this work can be found in the works of Ibrahimbegovic and Melnyk [33] in a 2D setting, and it is brought to a 3D environment in the works of Benkemoun et al. [34].

It is recognized by the authors of this study that a global approach for element enhancements has a broader field coherence and capacity for the representation of complex multiphasic material distributions. It is also observed that many authors working within the E-FEM framework have opted for a workaround by implementing global tracking algorithms, strongly linking the locally defined enhancements [35,36]. However, it has been the choice of the authors of this work to retain a *strictly local* approach for the developments presented for the E-FEM framework. It is considered worth the effort to keep the simplicity and hermeticity of these internal mathematical enhancements that leave the global finite element solution process almost untouched, granting a non-invasive framework that can be used within any standard finite element solution platform as a plain internal element routine, only returning local stiffness and residual contributions. It is the explicit intent of the authors to show the limits of such a local approach, discussing on both prediction quality and practicality of the framework.

A brief analysis on the evolution of the use of the weak discontinuity model on the E-FEM approach will be presented to the reader in Section 2. A detailed analysis of the theoretical foundations for the definition of weak discontinuity enhancements for the modelling of heterogeneous materials will be introduced in Section 3. This will help to establish a set of basic consistency requirements for defining these enhancements under the light of the Hu-Washizu variational framework. In Section 4, two particular weak discontinuity enhancement functions will be derived based on this consistency analysis and the amount of requirements chosen to be satisfied. The first of them is the one typically managed in the reference E-FEM works, and a second one is proposed to purposefully maximize variational and kinematic consistency.

Finally, numerical simulations are made to assess the performance of the weak discontinuity enhancement proposals, showing the reader overall how far a strictly local E-FEM approach can go in terms of the correct physical simulation of heterogeneous materials. First, the analytical solution for a simple bi-strip material model will serve as a reference to assess the basic performance of the enhancements. Afterwards, simulations involving a more realistic model having a number of inclusions within an homogeneous material matrix domain is performed to study more complex mesh sensitive phenomena. These last simulations are compared to a standard FEM model, which has its mesh completely adapted to the presence of the inclusions. A concluding discussion will follow in Section 6, considering all theoretical and practical aspects of the developments presented in this work.

2. The role of weak discontinuity enhancements on the E-FEM framework

The use of weak discontinuity enhancements started actually as one of the first embedded finite element approaches for the modelling of shear instability bands, with some pioneering studies paving the way for consolidating the E-FEM approach as a whole by authors such as Ortiz [37], Belytschko [38] and Sluys [39]. The main idea was to model a shear band through the use of two parallel strain discontinuity lines that would cross a non-adapted mesh, typically having a uniform geometry. The elements having sub-domains enclosed by the shear band would have different constitutive properties to represent the local instability happening inside. It introduces a jump on the strain field, which translates into a sudden change in slope for its corresponding displacement field without breaking its continuity (this is thus the reason of calling it a *weak discontinuity enhancement*). Fig. 1 shows an example for a constant stress triangle (CST) element. The localisation band model represents a finite and continuous region of a fracture process.

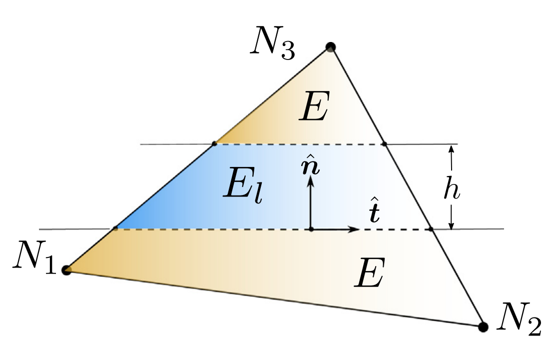

Fig. 1. Basic schematic of weak discontinuity enhancements used to represent a shear band within a triangular 2D element having a local frame $\hat{\boldsymbol{n}}, \hat{\boldsymbol{t}}$. The shear band possesses a set of different (damaged) mechanical properties E_l while the rest of the element retains its original elastic behvior E. Note the introduction of a thickness d characterising the shear band.

The weak discontinuity approach for this kind of material failure modelling got diversified afterwards with the introduction of regularization processes discussed by Simo, Oliver [40,41] to avoid scale dependencies, especially concerning the problem of setting an arbitrary shear band thickness. Eventually, attention was diverted towards the strong discontinuity enhancement equipped with a discrete post-localisation law as the method of choice for the modelling of internal element fracture on the E-FEM framework. It was at this stage that the detailed theoretical and implementation works of Oliver [21,42], Borja [43], Jirasek [20], Borst, Wells and Sluys [44] and Alfaiate and Dias da Costa [45] established a strong foundation for the E-FEM approach to thrive as an advanced finite element method. The tendency of this evolution was practically to drive the shear band model thickness to zero while maintaining mathematical and physical coherence on the formulation. This translates the discontinuity to the displacement field directly (thus the reason of naming it a *strong discontinuity*). The strong discontinuity enhancement was indeed proven to be a more pragmatic and robust way to avoid mesh dependencies as possible, granting more objectivity to the approach. Nonetheless, the application of embedded weak discontinuity enhancements for the modelling of shear bands still gathers some interest in recent works, such as ductile material failure simulations under dynamic conditions [46,47].

The interest of an effective and accurate modelling of local fractures through the use of strong discontinuities further continued by refining the mathematical definition of the embedded enhancements to avoid theoretical faults and increase modelling flexibility. As an example, the use of non-uniform strong discontinuity jump functions introduced and comprehensively studied in the works of Armero and Linder [48], Alfaiate, Simone and Sluys [49] allowed the introduction of new local fracture rotation modes that increased the kinematic consistency of the E-FEM formulation overall in a 2D context.

The use of an E-FEM approach to directly model different material phases, however, did not evolve at the same pace since they do not make use of an embedded strong discontinuity. The authors of this study consider that the application of weak discontinuity enhancements to model material heterogeneities really started with the works on fracture simulations of cementitious materials on the mesoscale [33,34,50]. These developments began by modeling a single weak discontinuity on 1-D beam elements to represent the presence of two different linear elastic stiffness domains coexisting on the same element. The perspective was different to that of Voronoi cell constructions [6] in the sense that no regular inclusion recognition had to be made on a material matrix to assign one beam per interface. A totally random, unstructured 3-D mesh was built with beam elements and a material heterogeneity distribution in space was just projected directly onto it. Some elements would fall entirely on the domain of one material phase or other, while others would be found in a region where there was an interface between materials. It is those elements that were enriched with a weak discontinuity enhancement function.

The model was also equipped with a strong discontinuity enhancement at the same location as the weak discontinuity to represent eventual failure and separation of the domains. In this sense, the work was also innovating from the perspective of integrating both discontinuity enhancements for entirely different roles. While this model allowed an explicit use of the weak discontinuity to finally model mesh-independent heterogeneities, no objective state of stresses was described in the domains as no spatially accurate representation of the continuum is possible by only making use of 1-D beam elements.

It was only with the work of Roubin [22] that this application of the weak discontinuity model was devised for 3-D elements, inspired on the works of Markovic [51,52]. The main idea was to establish a piece-wise displacement field enrichment that, once being processed through the application of a symmetrical gradient operator ∇^{sym}, it would comply with the Maxwell interface strain compatibility conditions [37]. The model counts with one, two or three internal variables characterising the strain jump between materials depending on the dimension of the problem. As his predecessors, Roubin also appended a strong discontinuity enhancement to integrate a fracture model, but only considering a single fracture kinematic mode: normal separation.

This 3-D development was later taken as a base by Hauseaux, Vallade, Stamati and Sun [53–56] to perform simulations for heterogeneous rocks and cementitious materials in a similar fashion. A variety of fracture phenomena was explored, such as plane sliding, crack reclosure and multi-scale analyses, among other developments. Further applications of these ideas can be found in the domain of poromechanics and electromechanics [57,58]. The use of the weak discontinuity on this format acquired yet more relevance with the recent works of Stamati et al. [59,55], where image processing techniques and X-ray tomography made possible to project realistic heterogeneity distributions coming from actual samples used for experimental campaigns, reaching a new level of predictability and model validation procedures.

All the aforementioned works concern linear element formulations having a constant stress field, which simplifies the mathematical works required to constitute such frameworks. The reader can find additional studies on non-constant stress field base elements in a 2D setting (such as a Q6 element) in the works of Stanic et al. [60,61].

This application of the weak discontinuity model for 3-D geometries, as seen in the work of Roubin [22], has been taken as the point of departure for the present study. In the next section, the theoretical basis behind it will be scrutinised in detail. To help the reader understand better the theoretical improvements proposed to the weak discontinuity formulation explained in Section 4, a selected summary of the fundamentals of embedded weak discontinuity formulations is provided. The reader can find a set of detailed explanations in a reference textbook by Ibrahimbegovic [62].

3. Theoretical foundations

The basic construction of a weak discontinuity for the modelling of material heterogeneities starts with the assumption that a heterogeneous displacement field $\boldsymbol{u}$, referred from now on to as the *physical* displacement, can be expressed as the composition of an average homogenized base field $\bar{\boldsymbol{u}}$ and a field enhancement $\tilde{\boldsymbol{u}}$ carrying the mathematical weak discontinuity:

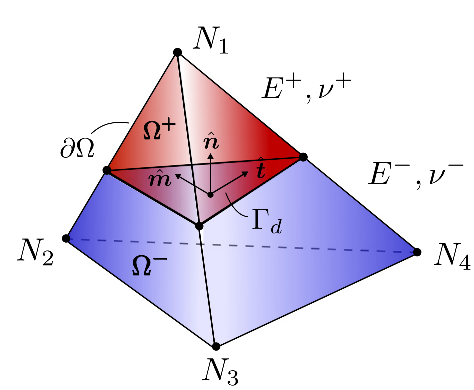

Fig. 2. Basic schematic of a weak discontinuity in 3-D for the modelling of material heterogeneities within a tetrahedral element.

$$\boldsymbol{u} = \overline{\boldsymbol{u}} + \widetilde{\boldsymbol{u}} \tag{1}$$

Fig. 2 illustrates a typical dual material partition for a 4-node tetrahedral element in domains Ω^+, Ω^- with a boundary $\partial\Omega$ and having a plane Γ_d as an interface. The base work by Roubin [22,63] considers linear elastic properties for each domain such as Young moduli E^+, E^- and Poisson ratios ν^+, ν^-. A local coordinate system $(\hat{\boldsymbol{n}}, \hat{\boldsymbol{t}}, \hat{\boldsymbol{m}})$ defines the orientation of the material interface, having $\hat{\boldsymbol{n}}$ as the unit vector normal to Γ_d.

The homogeneous base field $\overline{\boldsymbol{u}}$ is determined entirely by the displacement of the tetrahedral nodes and the natural interpolation functions of the element. The definition of the field $\widetilde{\boldsymbol{u}}$ is determined by internal variables keeping in mind that its corresponding strain function should introduce the strain jump associated with the change of material domains. The strain fields, as second order tensors, are obtained through a symmetric gradient operator $\nabla^s(\bullet) = \frac{1}{2}\left[\nabla(\bullet)^T + \nabla(\bullet)\right]$:

$$\boldsymbol{\varepsilon} = \nabla^s \boldsymbol{u} = \nabla^s \overline{\boldsymbol{u}} + \nabla^s \widetilde{\boldsymbol{u}} = \overline{\boldsymbol{\varepsilon}} + \widetilde{\boldsymbol{\varepsilon}} \tag{2a}$$
$$\boldsymbol{\varepsilon}^+ = \overline{\boldsymbol{\varepsilon}} + \widetilde{\boldsymbol{\varepsilon}}^+, \quad \boldsymbol{x} \in \Omega^+ \tag{2b}$$
$$\boldsymbol{\varepsilon}^- = \overline{\boldsymbol{\varepsilon}} + \widetilde{\boldsymbol{\varepsilon}}^-, \quad \boldsymbol{x} \in \Omega^- \tag{2c}$$

where a distinction has been done between the strain fields on the Ω^+ and Ω^- domains at each side of Γ_d. Note that the base field $\overline{\boldsymbol{\varepsilon}}$ remains invariant by the definition of $\overline{\boldsymbol{u}}$.

To retain kinematic and variational consistency, the weak discontinuity model has to comply with certain requirements through both displacement and strain fields. The approach in this study will be to determine the possible functions for the enhanced displacement field by introducing and applying these constraints, also noting the set of constraints effectively considered in the work of Roubin, Hauseux and Benkemoun [22,53,34] that shapes the most typical choice for it in those works.

From now on, the analysis will take place on the local reference frame $(\hat{\boldsymbol{n}}, \hat{\boldsymbol{t}}, \hat{\boldsymbol{m}})$ unless stated otherwise. Its coordinate variables will be denoted as ξ, η, ζ.

The most basic constraint pertains the physical displacement field $\boldsymbol{u}$: it shall not lose continuity through the material interface. Given that the base field $\overline{\boldsymbol{u}}$ is already continuous by definition, this implies that the enhanced displacement $\widetilde{\boldsymbol{u}}$ also has to be continuous:

$$\widetilde{\boldsymbol{u}}^+\big|_{\Gamma_d} = \widetilde{\boldsymbol{u}}^-\big|_{\Gamma_d} \tag{3}$$

The next involves an analysis of the strain field and the definition of the strain discontinuity jump. A strain discontinuity jump $\Delta\widetilde{\boldsymbol{\varepsilon}}$ is defined as the difference of strain fields $\widetilde{\boldsymbol{\varepsilon}}^+$ and $\widetilde{\boldsymbol{\varepsilon}}^-$ at the material interface Γ_d, resulting also in a second order tensor:

$$\Delta\widetilde{\boldsymbol{\varepsilon}} = \widetilde{\boldsymbol{\varepsilon}}^+\big|_{\Gamma_d} - \widetilde{\boldsymbol{\varepsilon}}^-\big|_{\Gamma_d} = \begin{bmatrix} \Delta\widetilde{\varepsilon}_{nn} & \Delta\widetilde{\varepsilon}_{nt} & \Delta\widetilde{\varepsilon}_{nm} \\ \text{sym} & \Delta\widetilde{\varepsilon}_{tt} & \Delta\widetilde{\varepsilon}_{tm} \\ \text{sym} & \text{sym} & \Delta\widetilde{\varepsilon}_{mm} \end{bmatrix} \tag{4}$$

The components of the strain jump $\Delta\widetilde{\boldsymbol{\varepsilon}}$ are not obliged to respect full continuity as their parent displacement field, but must still comply with Maxwell strain compatibility conditions [37] to be coherent with it. For this, the projection of $\Delta\widetilde{\boldsymbol{\varepsilon}}$ on the normal direction $\hat{\boldsymbol{n}}$ will be free of constraints, while all other unrelated components of the tensor will be driven down to zero. Recall that in a local coordinate setting, the projections can be easily obtained by just extracting the line-column corresponding to a given direction within the tensor. Thus:

$$\begin{aligned} \Delta\widetilde{\boldsymbol{\varepsilon}} \cdot \hat{\boldsymbol{n}} &= \begin{bmatrix} \Delta\widetilde{\varepsilon}_{nn} & \Delta\widetilde{\varepsilon}_{nt} & \Delta\widetilde{\varepsilon}_{nm} \end{bmatrix}^T \neq \boldsymbol{0} \\ \Delta\widetilde{\varepsilon}_{tt} &= \Delta\widetilde{\varepsilon}_{tm} = \Delta\widetilde{\varepsilon}_{mm} = 0 \end{aligned} \tag{5}$$

This leaves the strain jump tensor $\Delta\widetilde{\boldsymbol{\varepsilon}}$ with only three active components $\Delta\widetilde{\varepsilon}_{nn}, \Delta\widetilde{\varepsilon}_{nt}, \Delta\widetilde{\varepsilon}_{nm}$. These will be redefined as $[\varepsilon]_n, [\varepsilon]_t$ and $[\varepsilon]_m$, respectively. These are indeed the internal variables that define the weak discontinuity model. With this, a new enhancement requirement is defined:

$$\Delta\widetilde{\boldsymbol{\varepsilon}} = \widetilde{\boldsymbol{\varepsilon}}^+\big|_{\Gamma_d} - \widetilde{\boldsymbol{\varepsilon}}^-\big|_{\Gamma_d} = \begin{bmatrix} [\varepsilon]_n & [\varepsilon]_t & [\varepsilon]_m \\ [\varepsilon]_t & 0 & 0 \\ [\varepsilon]_m & 0 & 0 \end{bmatrix} \tag{6}$$

The requirements to follow need considerations coming from the variational analysis. As in [64,22,53] and in most of other works on the E-FEM framework, the Hu-Washizu variational principle is chosen due to its flexibility to handle element field enhancements through the independence of displacement, strain and stress fields. In a Voigt format, it can be expressed as:

$$_{\Omega}\partial\delta\boldsymbol{u}^t\boldsymbol{\sigma}\, dV - {}_{\Omega}\delta\boldsymbol{u}^t\boldsymbol{f}_b\, dV - {}_{\partial\Omega}\delta\boldsymbol{u}^t\boldsymbol{t}\, dA = 0 \tag{7a}$$
$$_{\Omega_e}\delta\boldsymbol{\sigma}^t(\partial\boldsymbol{u} - \boldsymbol{\varepsilon})dV = 0 \tag{7b}$$
$$_{\Omega_e}\delta\boldsymbol{\varepsilon}^t(\boldsymbol{\sigma}(\boldsymbol{\varepsilon}) - \boldsymbol{\sigma})dV = 0 \tag{7c}$$

where the real fields have been denoted as $(\boldsymbol{u}, \boldsymbol{\varepsilon}, \boldsymbol{\sigma})$ and the field variations (or *virtual* fields) as $(\delta\boldsymbol{u}, \delta\boldsymbol{\varepsilon}, \delta\boldsymbol{\sigma})$, having a boundary traction vector $\boldsymbol{t}$ and body forces $\boldsymbol{f}_b$. It is important to note that the real stress field $\boldsymbol{\sigma}$, in general, is different from the stress coming from constitutive law calculations $\boldsymbol{\sigma}(\boldsymbol{\varepsilon})$. The same can be said from the real strain field $\boldsymbol{\varepsilon}$ and $\partial\boldsymbol{u}$, where ∂ is the Voigt notation equivalent of the symmetric gradient operator ∇^s.

All fields are independent from each other, in the sense that they do not have to necessarily follow direct gradient relations such as in Eq. 2a. The Hu-Washizu variational principle allows for flexible field discretization strategies. However, the fields should retain enough physical meaningfulness to be able to correctly model the phenomenon in question. Authors working on this framework generally choose a discretisation strategy as to render the model as manageable and efficient as possible sacrificing the minimal amount of mechanical representation quality. This choice also considers the ease of an integration process with other models that might have a similar field discretisation approach (such as a strong discontinuity model).

The displacement and displacement variation fields $\boldsymbol{u}, \delta\boldsymbol{u}$ are commonly discretized taking only the standard displacement field $\overline{\boldsymbol{u}}$:

$$\boldsymbol{u} = \overline{\boldsymbol{u}} = \mathbf{N}\boldsymbol{d} \tag{8a}$$
$$\delta\boldsymbol{u} = \mathbf{N}\delta\boldsymbol{d} \tag{8b}$$

with $\mathbf{N}$ as a standard interpolation matrix and $\boldsymbol{d}$ the standard nodal displacement vector. $\delta\boldsymbol{d}$ is the corresponding variation. This strategy means that only the field $\overline{\boldsymbol{u}}$ is used for describing node positions and imposing boundary conditions. In such case, it should be clear that, in order to ensure that $\boldsymbol{d}$ retains the correct nodal information, the field $\overline{\boldsymbol{u}}$ should have the same value as $\boldsymbol{u}$ at the boundaries $\partial\Omega$ of all the element (i.e. the nodes on it):

$$\boldsymbol{u}\big|_{\partial\Omega} = \overline{\boldsymbol{u}}\big|_{\partial\Omega} \tag{9}$$

Given that we already have a definition as stated in Eq. 1, this implies:

$$\boldsymbol{u}\big|_{\partial\Omega} = \overline{\boldsymbol{u}}\big|_{\partial\Omega} + \widetilde{\boldsymbol{u}}\big|_{\partial\Omega} \Rightarrow \widetilde{\boldsymbol{u}}\big|_{\partial\Omega} = 0 \tag{10}$$

This analysis defines the next constraint for the weak discontinuity model:

$$\widetilde{\boldsymbol{u}}\big|_{\boldsymbol{x}=\boldsymbol{x}_i} = 0, \qquad i = 1, 2, \ldots, N_e \tag{11}$$

where $\boldsymbol{x}_i$ are nodal positions and N is the number of nodes of the element. This requirement stands as the most overlooked in the current literature of this family of formulations applied to the modelling of material heterogeneities. It is also the one that will make a significant difference in the enhancement function shape with respect to the one used in typical heterogeneous E-FEM studies. Going forward with the discretisation strategy, the domain dependent strain field $\boldsymbol{\varepsilon}$ and its variation $\delta\boldsymbol{\varepsilon}$ conserve all kinematics description terms as stated in Eqs. 2a,2b. Their enhanced sections ($\widetilde{\boldsymbol{\varepsilon}}$ and $\delta\widetilde{\boldsymbol{\varepsilon}}$, respectively), which depend on the internal variables $[\varepsilon]_n, [\varepsilon]_t, [\varepsilon]_m$, are stated through the definition of a *weak discontinuity vector* $[|\boldsymbol{\varepsilon}|] = [\,[\varepsilon]_n \quad [\varepsilon]_t \quad [\varepsilon]_m\,]^T$ and its variation $\delta[|\boldsymbol{\varepsilon}|]$. This discretisation strategy also allows to use different interpolation matrices $\mathbf{G}_w^{\pm}, \mathbf{G}_w^{*\pm}$ for the real and variation enhancements, respectively:

$$\boldsymbol{\varepsilon} = \begin{cases} \mathbf{B}\boldsymbol{d} + \mathbf{G}_w^{+}[|\boldsymbol{\varepsilon}|] & \boldsymbol{x} \in \Omega^{+} \\ \mathbf{B}\boldsymbol{d} + \mathbf{G}_w^{-}[|\boldsymbol{\varepsilon}|] & \boldsymbol{x} \in \Omega^{-} \end{cases} \tag{12a}$$

$$\delta\boldsymbol{\varepsilon} = \begin{cases} \mathbf{B}\delta\boldsymbol{d} + \mathbf{G}_w^{*+}\delta[|\boldsymbol{\varepsilon}|] & \boldsymbol{x} \in \Omega^{+} \\ \mathbf{B}\delta\boldsymbol{d} + \mathbf{G}_w^{*-}\delta[|\boldsymbol{\varepsilon}|] & \boldsymbol{x} \in \Omega^{-} \end{cases} \tag{12b}$$

Note that, until now, no specific form for $\mathbf{G}_w^{\pm}, \mathbf{G}_w^{*\pm}$ has been assigned yet. In the original work of Roubin [22], it is actually assumed that $\mathbf{G}_w^{\pm} = \mathbf{G}_w^{*\pm}$. The reason for this choice will be explained in Section 4.1. The matrix $\mathbf{B}$ remains a standard strain interpolation matrix involving the partial derivatives of the base element shape functions.

The stress field $\boldsymbol{\sigma}$ and its variation $\delta\boldsymbol{\sigma}$ are interpolated using single independent stress vectors $\boldsymbol{s}$and $\delta\boldsymbol{s}$ through the use of interpolation matrices $\mathbf{S}$ and $\mathbf{S}^*$, respectively:

$$\boldsymbol{\sigma} = \mathbf{S}\boldsymbol{s} \tag{13a}$$

$$\delta\boldsymbol{\sigma} = \mathbf{S}^*\delta\boldsymbol{s}, \tag{13b}$$

The definition for the stress field coming from the constitutive law $\boldsymbol{\sigma}(\boldsymbol{\varepsilon})$ is based on the assumption that each of the material domains possesses its own linear elastic constitutive law considering separate second order linear elastic constitutive tensors $\mathbf{C}^+$ and $\mathbf{C}^-$. These linear operators act upon different regions of the *real* strain field $\boldsymbol{\varepsilon}$. The definition for this stress field is thus devised as:

$$\boldsymbol{\sigma}(\boldsymbol{\varepsilon}) = \begin{cases} \mathbf{C}^{+}\left(\mathbf{B}\boldsymbol{d} + \mathbf{G}_w^{+}[|\boldsymbol{\varepsilon}|]\right) & \boldsymbol{x} \in \Omega^{+} \\ \mathbf{C}^{-}\left(\mathbf{B}\boldsymbol{d} + \mathbf{G}_w^{-}[|\boldsymbol{\varepsilon}|]\right) & \boldsymbol{x} \in \Omega^{-} \end{cases} \tag{14}$$

It should be emphasized that while the constitutive stress $\boldsymbol{\sigma}(\boldsymbol{\varepsilon})$ is by default a domain-dependent definition, the *real* stress field $\boldsymbol{\sigma}$ is not necessarily obliged to follow the same characteristics.

Having set a discretisation strategy, the variational analysis takes place by using all previous equations to develop the Hu-Washizus system through Eqs. (7a)–(7c). The detailed process of this variational analysis is lengthy and judged too technical by the authors of this work to be included in this manuscript. However, the reader can refer to the works done by Ortega Laborin et al. [65] to follow a step-by-step description and the assumptions made during this process, where the framework is being applied for the analysis of a strong discontinuity.

The requirement of passing a constant stress patch test [51,44] yields another requirement for the weak discontinuity model enhancements:

$$\int_{\Omega^+} \mathbf{G}_w^{*+T} dV + \int_{\Omega^-} \mathbf{G}_w^{*-T} dV = \mathbf{0} \tag{15}$$

The works in [22,63] take the simplest approach for a tetrahedron element, which is to assume a constant real stress field. This allows the possibility to make constant matrix definitions for $\mathbf{G}_w^{*\pm}$, yielding:

$$V^+\mathbf{G}_w^{*+} + V^-\mathbf{G}_w^{*-} = \mathbf{0} \tag{16}$$

A final relation for calculating the weak discontinuity internal variables $[\varepsilon]_n, [\varepsilon]_t, [\varepsilon]_m$ as a function of a displacement input $\boldsymbol{d}$ can be obtained from further working the Hu-Washizu system (Eqs. (7a)–(7c)) if a definite shape for all weak discontinuity enhancement matrix operators $\mathbf{G}_w^{\pm}$ and $\mathbf{G}_w^{*\pm}$ has been established at this point:

$$\mathbf{K}_{wb}\boldsymbol{d} + \mathbf{K}_{ww}[|\boldsymbol{\varepsilon}|] = \mathbf{0} \tag{17a}$$

$$\mathbf{K}_{wb} = \int_{\Omega^+} \mathbf{G}_w^{*+T}\mathbf{C}^+\mathbf{B}dV + \int_{\Omega^-} \mathbf{G}_w^{*-T}\mathbf{C}^-\mathbf{B}dV \tag{17b}$$

$$\mathbf{K}_{ww} = \int_{\Omega^+} \mathbf{G}_w^{*+T}\mathbf{C}^+\mathbf{G}_w^{+}dV + \int_{\Omega^-} \mathbf{G}_w^{*-T}\mathbf{C}^-\mathbf{G}_w^{-}dV \tag{17c}$$

$$[|\boldsymbol{\varepsilon}|] = \mathbf{K}_{ww}^{-1}\mathbf{K}_{wb}\boldsymbol{d}, \tag{17d}$$

where specific enhancement stiffness matrices $\mathbf{K}_{wb}, \mathbf{K}_{ww}$ have been defined.

4. Weak discontinuity enhancement proposals

Now that all relevant constraints for defining weak enhancement functions have been introduced, a particularisation of the model will take place, deriving two different enhancement field functions considering slightly different ways of achieving the satisfaction of consistency requirements. For the sake of simplicity and coherence with the background literature, a linear tetrahedron will be set as the base element from now on. For now, it will be assumed that a constant stress field $\boldsymbol{\sigma}$ is sought.

4.1. Typical enhancement analysis

Authors managing the modelling approach in [22,63] decided to make the weak discontinuity enhancement completely symmetrical by letting $\mathbf{G}_w^{\pm} = \mathbf{G}_w^{*\pm}$. This automatically renders the weak discontinuity model variationally symmetric at the expense of removing the flexibility of having a virtual enhancement with different characteristics. At the same time, only requirements 1, 2 and 4 (Eqs. 3, 6, 15) are explicitly imposed to this unique enhancement function. Instead of requirement 3 (Eq. 11), a general zero reference for the enhancement is set at the interface plane Γ_d. This last imposition is absolutely unrelated to any considerations on variational consistency. This line of approach also chooses the simplest definition for the model: a linear field $\widetilde{\boldsymbol{u}}$ and therefore constant operators $\mathbf{G}_w^{\pm}$.

Considering these restrictions, it will be demonstrated that the possible function space for $\widetilde{\boldsymbol{u}}$ reduces to a unique expression. Let the following linear definitions for the piece-wise enhanced displacement field be:

$$\widetilde{\boldsymbol{u}}^+ = \boldsymbol{a}^+ + \boldsymbol{b}^+\xi + \boldsymbol{c}^+\eta + \boldsymbol{d}^+\zeta \tag{18a}$$

$$\widetilde{\boldsymbol{u}}^- = \boldsymbol{a}^- + \boldsymbol{b}^-\xi + \boldsymbol{c}^-\eta + \boldsymbol{d}^-\zeta \tag{18b}$$

where each vector has components contributing to each local direction $(\hat{\boldsymbol{n}}, \hat{\boldsymbol{t}}, \hat{\boldsymbol{m}})$, *e.g.*, $\widetilde{\boldsymbol{u}}^+ = [\,\widetilde{u}_n^+ \quad \widetilde{u}_t^+ \quad \widetilde{u}_m^+\,]^T$. The goal is to particularize the vectors $\boldsymbol{a}^{\pm}, \boldsymbol{b}^{\pm}, \boldsymbol{c}^{\pm}, \boldsymbol{d}^{\pm}$ as a function of basic element data and the weak discontinuity variables $[|\varepsilon|]_n, [|\varepsilon|]_t$ and $[|\varepsilon|]_m$. In local coordinates, it is not hard to see that the interface plane Γ_d is simply described by the equation $\xi = 0$. This eases the application of requirement 1:

$$\widetilde{\boldsymbol{u}}^+\big|_{\xi=0} = \widetilde{\boldsymbol{u}}^-\big|_{\xi=0} \tag{19a}$$

$$\boldsymbol{a}^+ + \boldsymbol{c}^+\eta + \boldsymbol{d}^+\zeta = \boldsymbol{a}^- + \boldsymbol{c}^-\eta + \boldsymbol{d}^-\zeta \tag{19b}$$

$$\Rightarrow \boldsymbol{a}^+ = \boldsymbol{a}^- = \boldsymbol{a},\ \boldsymbol{c}^+ = \boldsymbol{c}^- = \boldsymbol{c},\ \boldsymbol{d}^+ = \boldsymbol{d}^- = \boldsymbol{d} \tag{19c}$$

where the $\pm$ will be omitted from now on in all coefficients $\boldsymbol{a}, \boldsymbol{c}, \boldsymbol{d}$.

The strain jump requirement (Eq. 6) requires the calculation of the symmetric gradients on each part of the enhanced displacement field:

$$\widetilde{\boldsymbol{\varepsilon}}^+ - \widetilde{\boldsymbol{\varepsilon}}^- = \begin{bmatrix} [\varepsilon]_n & [\varepsilon]_t & [\varepsilon]_m \\ [\varepsilon]_t & 0 & 0 \\ [\varepsilon]_m & 0 & 0 \end{bmatrix} \tag{20a}$$

$$\widetilde{\boldsymbol{\varepsilon}}^\pm = \begin{bmatrix} b_n^\pm & \frac{1}{2}\left(c_n + b_t^\pm\right) & \frac{1}{2}\left(d_n + b_m^\pm\right) \\ \text{sym} & c_t & \frac{1}{2}(d_t + c_m) \\ \text{sym} & \text{sym} & d_m \end{bmatrix} \tag{20b}$$

$$\widetilde{\boldsymbol{\varepsilon}}^+ - \widetilde{\boldsymbol{\varepsilon}}^- = \begin{bmatrix} b_n^+ - b_n^- & \frac{1}{2}(b_t^+ - b_t^-) & \frac{1}{2}(b_m^+ - b_m^-) \\ \frac{1}{2}(b_t^+ - b_t^-) & 0 & 0 \\ \frac{1}{2}(b_m^+ - b_m^-) & 0 & 0 \end{bmatrix} \tag{20c}$$

$$\Rightarrow [|\boldsymbol{\varepsilon}|] = \begin{bmatrix} [|\varepsilon]_n \\ [|\varepsilon]_t \\ [|\varepsilon]_m \end{bmatrix} = \begin{bmatrix} b_n^+ - b_n^- \\ \frac{1}{2}(b_t^+ - b_t^-) \\ \frac{1}{2}(b_m^+ - b_m^-) \end{bmatrix} \tag{20d}$$

Here, the results of Eq. 19c have been used. Note that for this reason, the zeros required in the strain jump matrix are produced naturally.

The application of the patch test (Eq. 15) becomes easier if both sides of Eq. 16 are multiplied (contracted) by the weak discontinuity variable vector $[|\boldsymbol{\varepsilon}|]$ to recover enhanced strain fields, but in vector format:

$$V^+ \underbrace{\mathbf{G}_w^+[|\boldsymbol{\varepsilon}|]}_{\widetilde{\boldsymbol{\varepsilon}}^+} + V^- \underbrace{\mathbf{G}_w^-[|\boldsymbol{\varepsilon}|]}_{\widetilde{\boldsymbol{\varepsilon}}^-} = \mathbf{0}[|\boldsymbol{\varepsilon}|] = \mathbf{0} \tag{21a}$$

$$V^+ \begin{bmatrix} b_n^+ \\ c_t \\ d_m \\ \frac{1}{2}(c_n + b_t^+) \\ \frac{1}{2}(d_t + c_m) \\ \frac{1}{2}(d_n + b_m^+) \end{bmatrix} = -V^- \begin{bmatrix} b_n^- \\ c_t \\ d_m \\ \frac{1}{2}(c_n + b_t^-) \\ \frac{1}{2}(d_t + c_m) \\ \frac{1}{2}(d_n + b_m^-) \end{bmatrix} \tag{21b}$$

$$\Rightarrow c_t = d_m = 0 \tag{21c}$$

Afterwards, the original idea for this formulation coming from Markovic [51] involves the imposition of a requirement that is *not mandatory* for variational consistency. The enhanced displacement $\widetilde{\boldsymbol{u}}$ is prescribed with a value of zero through all the interface plane ($\xi = 0$). While Markovic did never reveal any particular reasons for this decision in his research, it is later found in this work through further mathematical analysis (Sections 4.3, 4.4, 4.5) that this constraint provides some operational benefits to the framework. Indeed, the imposition of a zero enhanced displacement reference at Γ_d is an aggressive constraint that will simplify the enhancement function to a great extent:

$$u^+|_{\xi=0} = u^-|_{\xi=0} = 0 \tag{22a}$$

$$\begin{bmatrix} a_n \\ a_t \\ a_m \end{bmatrix} + \begin{bmatrix} c_n \\ 0 \\ c_m \end{bmatrix}\eta + \begin{bmatrix} d_n \\ d_t \\ 0 \end{bmatrix}\zeta = \begin{bmatrix} 0 \\ 0 \\ 0 \end{bmatrix} \tag{22b}$$

$$\Rightarrow \begin{bmatrix} a_n \\ a_t \\ a_m \end{bmatrix} = \begin{bmatrix} 0 \\ 0 \\ 0 \end{bmatrix}, \begin{bmatrix} c_n \\ 0 \\ c_m \end{bmatrix} = \begin{bmatrix} 0 \\ 0 \\ 0 \end{bmatrix}, \begin{bmatrix} d_n \\ d_t \\ 0 \end{bmatrix} = \begin{bmatrix} 0 \\ 0 \\ 0 \end{bmatrix} \tag{22c}$$

It should not be forgotten that this condition *is not* a replacement of requirement 3 (Eq. 11). With these results and the expressions coming from the application of the patch test requirement (Eq. 21b), one can calculate the $\boldsymbol{b}$ coefficients directly as a function of weak discontinuity internal variables:

$$b_n^+ = \frac{V^-}{V}[\varepsilon]_n,\; b_t^+ = 2\frac{V^-}{V}[\varepsilon]_t,\; b_m^+ = 2\frac{V^-}{V}[\varepsilon]_m \tag{23a}$$

$$b_n^- = -\frac{V^+}{V}[\varepsilon]_n,\; b_t^- = -2\frac{V^+}{V}[\varepsilon]_t,\; b_m^- = -2\frac{V^+}{V}[\varepsilon]_m \tag{23b}$$

In the end, the enhancement function reduces to just a set of $\boldsymbol{b}$ coefficients multiplying the coordinate ξ, which is the normal distance from the interface plane Γ_d:

$$\begin{bmatrix} \widetilde{u}_n^\pm \\ \widetilde{u}_t^\pm \\ \widetilde{u}_m^\pm \end{bmatrix} = \begin{bmatrix} b_n^\pm \\ b_t^\pm \\ b_m^\pm \end{bmatrix}\xi = \pm\frac{V^\mp}{V}\begin{bmatrix} [\varepsilon]_n \\ 2[\varepsilon]_t \\ 2[\varepsilon]_m \end{bmatrix}\xi \tag{24a}$$

$$\Rightarrow \widetilde{\boldsymbol{u}}^\pm = \pm\frac{V^\mp}{V}\xi\left([\varepsilon]_n\hat{\boldsymbol{n}} + 2[\varepsilon]_t\hat{\boldsymbol{t}} + 2[\varepsilon]_m\hat{\boldsymbol{m}}\right) \tag{24b}$$

If this expression is reverted to global coordinates, the original weak discontinuity enhancement version as used in Roubin [22] is recovered:

$$\widetilde{\boldsymbol{u}} = \Theta\hat{\boldsymbol{n}}\cdot\left(\boldsymbol{x} - \boldsymbol{x}_{\Gamma_d}\right)\left([\varepsilon]_n\hat{\boldsymbol{n}} + 2[\varepsilon]_t\hat{\boldsymbol{t}} + 2[\varepsilon]_m\hat{\boldsymbol{m}}\right) \tag{25}$$

$$\Theta = \begin{cases} \Theta^+ = \frac{V^-}{V} & \boldsymbol{x}\in\Omega^+ \\ \Theta^- = -\frac{V^+}{V} & \boldsymbol{x}\in\Omega^- \end{cases} \tag{26}$$

Here, the coordinate ξ has been expressed as a projection of a distance with respect to the Γ_d plane and a domain-dependent scalar Θ containing the volume ratios has been defined. It is important to note that the intent of this work to derive this already-known enhancement field shape is to demonstrate that, instead of starting with a seemingly arbitrary definition [51,22], its final form comes rather from the application of a definite set of constraints. This sheds light on the theoretical basis on which this family of enhancements is built upon.

From Eq. 25, general expressions for the $\mathbf{G}_w^\pm$ operators can be found on the global reference frame by applying the symmetrical gradient operator in global coordinates. Einstein index notation is useful to reach the following typical strain field tensor expression in terms of symmetric tensor products:

$$\widetilde{\boldsymbol{\varepsilon}} = \Theta\left[[\varepsilon]_n(\hat{\boldsymbol{n}}\otimes\hat{\boldsymbol{n}})^s + 2[\varepsilon]_m(\hat{\boldsymbol{n}}\otimes\hat{\boldsymbol{m}})^s + 2[\varepsilon]_t(\hat{\boldsymbol{n}}\otimes\hat{\boldsymbol{t}})^s\right], \tag{27}$$

This expression is converted into a Voigt format to finally obtain:

$$\widetilde{\boldsymbol{\varepsilon}} = \mathbf{G}_w^\pm[|\boldsymbol{\varepsilon}|] = \Theta\mathbf{H}_w[|\boldsymbol{\varepsilon}|]$$

$$\mathbf{H}_w = \begin{bmatrix} n_x^2 & n_x m_x & n_x t_x \\ n_y^2 & n_y m_y & n_y t_y \\ n_z^2 & n_z m_z & n_z t_z \\ n_x n_y + n_y n_x & n_x m_y + n_y m_x & n_x t_y + n_y t_x \\ n_z n_y + n_y n_z & n_z m_y + n_y m_z & n_z t_y + n_y t_z \\ n_z n_x + n_x n_z & n_z m_x + n_x m_z & n_z t_x + n_x t_z \end{bmatrix} \tag{28}$$

Note that the domain-dependent term in all these definitions stands as a single scalar Θ taking the form of domain volume ratios.

4.2. Consistent enhancement analysis

For the case of a more variationally consistent enhancement field considering requirement 3 (Eq. 11), it is more practical to start the analysis by expressing the enhancement as a piece-wise definition of two linear fields using classical linear interpolation functions:

$$\widetilde{\boldsymbol{u}}^+ = \widetilde{\boldsymbol{u}}_1^+\phi_1 + \widetilde{\boldsymbol{u}}_2^+\phi_2 + \widetilde{\boldsymbol{u}}_3^+\phi_3 + \widetilde{\boldsymbol{u}}_4^+\phi_4 \tag{29a}$$

$$\widetilde{\boldsymbol{u}}^- = \widetilde{\boldsymbol{u}}_1^-\phi_1 + \widetilde{\boldsymbol{u}}_2^-\phi_2 + \widetilde{\boldsymbol{u}}_3^-\phi_3 + \widetilde{\boldsymbol{u}}_4^-\phi_4 \tag{29b}$$

where the interpolation functions ϕ associated each node i of a base linear tetrahedron have been defined as $\phi_i = a_i + b_i\xi + c_i\eta + d_i\zeta$, where all coefficients a_i, b_i, c_i, d_i are known. This time, the goal of the model particularisation is to find the value of all the nodal enhanced displacements $\widetilde{\boldsymbol{u}}_i^\pm$ as a function of nodal coordinate information and weak discontinuity internal variables.

An auxiliary variable p_i is defined as a position indicator between the Ω^+ and the Ω^- domains as follows:

$$p_i = \begin{cases} 1 & \boldsymbol{x}_i \in \Omega^+ \\ 0 & \boldsymbol{x}_i \in \Omega^- \end{cases} \qquad i = \{1,2,3,4\} \tag{30}$$

Using this variable, a general *mixed* velocity variable $\widetilde{\boldsymbol{u}}_i$ is defined:

$$\widetilde{\boldsymbol{u}}_i = (1-p_i)\widetilde{\boldsymbol{u}}_i^+ + p_i\widetilde{\boldsymbol{u}}_i^-, \qquad i = \{1,2,3,4\} \tag{31}$$

Having all that, we can start by the application of requirement 3 (Eq. 11) in a very straight-forward fashion by just nullifying some nodal enhanced displacements in their corresponding domains. This leads to:

$$\widetilde{\boldsymbol{u}}^+ = \sum_i^N (1-p_i)\widetilde{\boldsymbol{u}}_i^+\phi_i \tag{32a}$$

$$\widetilde{\boldsymbol{u}}^- = \sum_i^N p_i\widetilde{\boldsymbol{u}}_i^-\phi_i \tag{32b}$$

This also implies that the mixed variable $\widetilde{\boldsymbol{u}}_i$ actually *captures the set of all* **non-zero** $\widetilde{\boldsymbol{u}}_i^\pm$ *variables to be solved* for in this process.

Next, displacement continuity (requirement 1) is applied:

$$\widetilde{\boldsymbol{u}}^+\big|_{\xi=0} = \widetilde{\boldsymbol{u}}^-\big|_{\xi=0} \tag{33a}$$

$$\sum_i^N (1-p_i)\widetilde{\boldsymbol{u}}_i^+(a_i + c_i\eta + d_i\zeta) = \sum_i^N p_i\widetilde{\boldsymbol{u}}_i^-(a_i + c_i\eta + d_i\zeta) \tag{33b}$$

where the mixed variable $\widetilde{\boldsymbol{u}}_i$ can be used to reach the following:

$$\sum_i^N (1-2p_i)a_i\widetilde{\boldsymbol{u}}_i = 0 \qquad \sum_i^N (1-2p_i)c_i\widetilde{\boldsymbol{u}}_i = 0 \qquad \sum_i^N (1-2p_i)d_i\widetilde{\boldsymbol{u}}_i = 0 \tag{34}$$

The strain jump requirement 2 follows exactly the same process followed previously in Eqs. 20a–20d to find expressions relating enhanced nodal displacements to weak discontinuity internal variables:

$$\sum_i^N b_i\widetilde{u}_{in} = [\varepsilon]_n \qquad \sum_i^N b_i\widetilde{u}_{it} = 2[\varepsilon]_t \qquad \sum_i^N b_i\widetilde{u}_{im} = 2[\varepsilon]_m \tag{35}$$

where $\widetilde{u}_{in}, \widetilde{u}_{it}, \widetilde{u}_{im}$ are the three components of each non-zero $\widetilde{\boldsymbol{u}}_i$ on the local directions associated to each node i.

At this point, it's worth stopping to make a variable summary on the linear system being currently built for all non-zero enhanced nodal displacements $\widetilde{\boldsymbol{u}}_i$. All non-zero variables corresponding to each direction $\hat{\boldsymbol{n}}, \hat{\boldsymbol{t}}, \hat{\boldsymbol{m}}$ can be grouped in single vectors $\widetilde{\boldsymbol{u}}_n, \widetilde{\boldsymbol{u}}_t, \widetilde{\boldsymbol{u}}_m$ as follows:

$$\widetilde{\boldsymbol{u}}_n = \begin{bmatrix} \widetilde{u}_{1n} \\ \widetilde{u}_{2n} \\ \widetilde{u}_{3n} \\ \widetilde{u}_{4n} \end{bmatrix}, \widetilde{\boldsymbol{u}}_t = \begin{bmatrix} \widetilde{u}_{1t} \\ \widetilde{u}_{2t} \\ \widetilde{u}_{3t} \\ \widetilde{u}_{4t} \end{bmatrix}, \widetilde{\boldsymbol{u}}_m = \begin{bmatrix} \widetilde{u}_{1m} \\ \widetilde{u}_{2m} \\ \widetilde{u}_{3m} \\ \widetilde{u}_{4m} \end{bmatrix} \tag{36}$$

The system can then be summarized using block matrix definitions:

$$\begin{bmatrix} \mathbf{C}_e & \boldsymbol{0}_4 & \boldsymbol{0}_4 \\ \boldsymbol{0}_4 & \mathbf{C}_e & \boldsymbol{0}_4 \\ \boldsymbol{0}_4 & \boldsymbol{0}_4 & \mathbf{C}_e \end{bmatrix} \begin{bmatrix} \widetilde{\boldsymbol{u}}_n \\ \widetilde{\boldsymbol{u}}_t \\ \widetilde{\boldsymbol{u}}_m \end{bmatrix} = \begin{bmatrix} [\boldsymbol{\varepsilon}]_{n,e} \\ [\boldsymbol{\varepsilon}]_{m,e} \\ [\boldsymbol{\varepsilon}]_{t,e} \end{bmatrix}, \tag{37}$$

where:

$$\mathbf{C}_e = \begin{bmatrix} (1-2p_1)a_1 & (1-2p_2)a_2 & (1-2p_3)a_3 & (1-2p_4)a_4 \\ (1-2p_1)b_1 & (1-2p_2)b_2 & (1-2p_3)b_3 & (1-2p_4)b_4 \\ (1-2p_1)c_1 & (1-2p_2)c_2 & (1-2p_3)c_3 & (1-2p_4)c_4 \\ (1-2p_1)d_1 & (1-2p_2)d_2 & (1-2p_3)d_3 & (1-2p_4)d_4 \end{bmatrix} \tag{38a}$$

$$\boldsymbol{0}_4 = \begin{bmatrix} 0 & 0 & 0 & 0 \\ 0 & 0 & 0 & 0 \\ 0 & 0 & 0 & 0 \\ 0 & 0 & 0 & 0 \end{bmatrix} \tag{38b}$$

$$[\boldsymbol{\varepsilon}]_{n,e} = \begin{bmatrix} 0 \\ [\varepsilon]_n \\ 0 \\ 0 \end{bmatrix}, [\boldsymbol{\varepsilon}]_{t,e} = 2\begin{bmatrix} 0 \\ [\varepsilon]_t \\ 0 \\ 0 \end{bmatrix}, [\boldsymbol{\varepsilon}]_{m,e} = 2\begin{bmatrix} 0 \\ [\varepsilon]_m \\ 0 \\ 0 \end{bmatrix} \tag{38c}$$

The system already counts with 12 enhanced nodal displacement variables and 12 equations, which render it closed with a unique solution if the coefficient matrix in Eq. 37 is not singular. Further application of requirement 4 (the patch test) *does not* add any new variables to the system. Therefore, it can be stated that for a linear definition of the enhanced field $\widetilde{\boldsymbol{u}}$, it is **not possible** to make a variationally symmetric definition for the $\mathbf{G}_w$ matrix operators having a unique base enhanced displacement field. To be fully consistent while keeping linear definitions, the framework requires to make $\mathbf{G}_w \neq \mathbf{G}_w^*$, taking requirement 4 (Eq. 15) as the guidance to define $\mathbf{G}_w^*$ and the other requirements to define $\mathbf{G}_w$ in a separate way. The typical weak discontinuity enhanced field (Eq. 25.) thus cannot be, by definition, variationally consistent.

The analysis on this section will continue to particularize the enhanced field with the system proposed in Eq. 37. As the system is block-diagonal, a compact-closed solution is found:

$$\widetilde{\boldsymbol{u}}_n = \begin{bmatrix} C_{1,2}^{-1} \\ C_{2,2}^{-1} \\ C_{3,2}^{-1} \\ C_{4,2}^{-1} \end{bmatrix}[\varepsilon]_n, \ \widetilde{\boldsymbol{u}}_t = 2\begin{bmatrix} C_{1,2}^{-1} \\ C_{2,2}^{-1} \\ C_{3,2}^{-1} \\ C_{4,2}^{-1} \end{bmatrix}[\varepsilon]_t, \ \widetilde{\boldsymbol{u}}_m = 2\begin{bmatrix} C_{1,2}^{-1} \\ C_{2,2}^{-1} \\ C_{3,2}^{-1} \\ C_{4,2}^{-1} \end{bmatrix}[\varepsilon]_m \tag{39}$$

where the $C_{i,2}^{-1}$ coefficients come from the second column of the inverse of the $\mathbf{C}_e$ matrix. The particularized enhanced field can then be expressed as:

$$\widetilde{\boldsymbol{u}}^+ = \sum_i^{N_e}(1-p_i)C_{i,2}^{-1}\phi_i\begin{bmatrix} [\varepsilon]_n \\ 2[\varepsilon]_t \\ 2[\varepsilon]_m \end{bmatrix} \qquad \widetilde{\boldsymbol{u}}^- = \sum_i^{N_e}p_iC_{i,2}^{-1}\phi_i\begin{bmatrix} [\varepsilon]_n \\ 2[\varepsilon]_t \\ 2[\varepsilon]_m \end{bmatrix} \tag{40}$$

Finally, the consistent weak enhancement field can still be written in the familiar format:

$$\widetilde{\boldsymbol{u}} = \Theta\left([\varepsilon]_n\hat{\boldsymbol{n}} + 2[\varepsilon]_t\hat{\boldsymbol{m}} + 2[\varepsilon]_m\hat{\boldsymbol{t}}\right) \tag{41}$$

$$\Theta = \begin{cases} \Theta^+ = \sum_i^{N_e}(1-p_i)C_{i,2}^{-1}\phi_i & x \in \Omega^+ \\ \Theta^- = \sum_i^{N_e}p_iC_{i,2}^{-1}\phi_i & x \in \Omega^- \end{cases} \tag{42}$$

It's important to note that, while Θ stays as a constant in the typical enhancement model, it becomes a variable parameter on the consistent model depending on nodal coordinates embedded in the interpolation functions ϕ_i.

The $\mathbf{G}_w^\pm$ operators can be devised again by making use of the symmetric gradient operator. Taking, for instance, the enhanced strain field on the Ω^+ domain one can reach an analogous tensor expression to that of the typical model:

$$\widetilde{\boldsymbol{\varepsilon}}^+ = \sum_i^{N_e}(1-p_i)C_{i,2}^{-1}\left[[\varepsilon]_n(\boldsymbol{e}_i\otimes\hat{\boldsymbol{n}})^s + 2[\varepsilon]_t(\boldsymbol{e}_i\otimes\hat{\boldsymbol{m}})^s + 2[\varepsilon]_t(\boldsymbol{e}_i\otimes\hat{\boldsymbol{t}})^s\right] \tag{43a}$$

$$\boldsymbol{e}_i = [\,b_i \quad c_i \quad d_i\,]^T \tag{43b}$$

Here, the vector $\boldsymbol{e}_i$ coming from *local* interpolation function coefficients, has to be transformed (rotated) to global coordinates as needed. Again, expressing in a Voigt vector field format:

$$\widetilde{\boldsymbol{\varepsilon}}^+ = \mathbf{G}_w^+[|\boldsymbol{\varepsilon}|] = \sum_i^{N_e}(1-p_i)C_{i,2}^{-1}\boldsymbol{H}_{W,i}[|\varepsilon|] \tag{44a}$$

$$\boldsymbol{H}_{W,i} = \begin{bmatrix} b_in_x & b_im_x & b_it_x \\ c_in_y & c_im_y & c_it_y \\ d_in_z & d_im_z & d_it_z \\ b_in_y+c_in_x & b_im_y+c_im_x & b_it_y+c_it_x \\ d_in_y+c_in_z & d_im_y+c_im_z & d_it_y+c_it_z \\ d_in_x+b_in_z & d_im_x+b_im_z & d_it_x+b_it_z \end{bmatrix} \tag{44b}$$

where the coefficients b_i, c_i, d_i are already taken from a rotated $\boldsymbol{e}_i$ vector in this global definition. $\mathbf{G}_w^-$ follows in a similar way:

$$\widetilde{\boldsymbol{\varepsilon}}^- = \mathbf{G}_w^-[|\boldsymbol{\varepsilon}|] = p_iC_{i,2}^{-1}\boldsymbol{H}_{W,i}[|\varepsilon|] \tag{45}$$

The virtual operators $\mathbf{G}_w^{*\pm}$ only have the goal of complying with the patch test (requirement 4). If the simplest, constant definition for them is adopted, satisfaction of Eq. 16 allows an infinite amount of choices. $\mathbf{G}_w^{*\pm}$ can, for instance, take the form of the typical enhancement (Eq. 28), which has been already built to satisfy Eq. 16.

4.3. Discussion on enhancement stability properties

The stability of the weak discontinuity model can be assessed by observing that in Eq. 17d, the calculation of the weak discontinuity variables $[\varepsilon]_t, [\varepsilon]_t, [\varepsilon]_m$ as a function of nodal standard displacements $\boldsymbol{d}$ depends on the inverse of a $\mathbf{K}_{ww}$ stiffness matrix. The behavior of $\mathbf{K}_{ww}$, depending on the form of the enhancement operators, will determine if the formulation becomes unstable under certain conditions. No other mathematical stability sources are identified.

For a more direct analysis, it is convenient to work in the local frame $(\hat{\boldsymbol{n}}, \hat{\boldsymbol{t}}, \hat{\boldsymbol{m}})$. It will be assumed that the consistent enhancement will use the same operators $\mathbf{G}_w^{*\pm}$ as the typical enhancement, while retaining the real operators $\mathbf{G}_w^{\pm}$ as devised in Section 4.2. If this is the case, both formulations will share the same $\mathbf{H}_w$ operator for virtual fields, which in local coordinates reduces to:

$$\mathbf{H}_w^T = \begin{bmatrix} 1 & 0 & 0 & 0 & 0 & 0 \\ 0 & 0 & 0 & 1 & 0 & 0 \\ 0 & 0 & 0 & 0 & 0 & 1 \end{bmatrix} \tag{46}$$

For a typical weak discontinuity enhancement, Eq. 17c can be developed to get to the following:

$$\mathbf{K}_{ww} = \frac{V^+V^-}{V^2}\mathbf{H}_w^T(\mathbf{C}^+V^- + \mathbf{C}^-V^+)\mathbf{H}_w, \tag{47}$$

where linear elastic constitutive matrices in three dimensions can be assumed for the corresponding materials on Ω^+ and Ω^- as:

$$\mathbf{C}^\pm = \begin{bmatrix} c_1^\pm & c_2^\pm & c_2^\pm & 0 & 0 & 0 \\ c_2^\pm & c_1^\pm & c_2^\pm & 0 & 0 & 0 \\ c_2^\pm & c_2^\pm & c_1^\pm & 0 & 0 & 0 \\ 0 & 0 & 0 & c_s^\pm & 0 & 0 \\ 0 & 0 & 0 & 0 & c_s^\pm & 0 \\ 0 & 0 & 0 & 0 & 0 & c_s^\pm \end{bmatrix} \tag{48}$$

for some real, positive constants $c_1^\pm, c_2^\pm, c_s^\pm$. Taking these definitions, the $\mathbf{K}_{ww}$ matrix associated to the typical enhancement can be calculated in a diagonal, compact expression:

$$\mathbf{K}_{ww} = \begin{bmatrix} V^+c_1^+ + V^-c_1^- & 0 & 0 \\ 0 & V^+c_s^+ + V^-c_s^- & 0 \\ 0 & 0 & V^+c_s^+ + V^-c_s^- \end{bmatrix} \tag{49}$$

As the constants $c_1^\pm, c_s^\pm$ stay real and positive as well as the subvolumes V^+, V^-, Eq. 49 reveals that the typical weak discontinuity enhancement turns out to be **unconditionally stable**, no matter what the orientation of the interface, the subvolume partition and the material elasticity characteristics are. By unconditional stability, the authors of this work mean that the solution for the weak discontinuity internal variable vector $[|\boldsymbol{\varepsilon}|]$ given by Eq. 17d does always exist given that the matrix $\mathbf{K}_{ww}$ remains invertible. This is the main reason why, despite not being variationally consistent by definition, authors in [22,53,55] have been keen to keep it on their heterogeneity modelling approaches, as it eases the implementation process and the numerical solution control.

Working with the consistent enhancement, Eq. 17c returns the following expression:

$$\mathbf{K}_{ww} = \frac{V^+V^-}{V}\mathbf{H}_w^T\sum_i^{N_e}C_{i,2}^{-1}\left[(1-p_i)\mathbf{C}^+ - p_i\mathbf{C}^-\right]\mathbf{H}_{w,i} \tag{50}$$

where the node-dependant matrix $\mathbf{H}_{wi}$ can be reduced to:

$$\mathbf{H}_{wi}^T = \begin{bmatrix} b_i & 0 & 0 & c_i & 0 & d_i \\ 0 & c_i & 0 & b_i & d_i & 0 \\ 0 & 0 & d_i & 0 & c_i & b_i \end{bmatrix} \tag{51}$$

Taking the same constitutive matrix definitions in Eq. 48, the $\mathbf{K}_{ww}$ for this case can be devised as:

$$\mathbf{K}_{ww} = \frac{V^+V^-}{V}\sum_i^{N_e}C_{i,2}^{-1}\begin{bmatrix} b_ik_{1i} & c_ik_{2i} & d_ik_{2i} \\ c_ik_{si} & b_ik_{si} & 0 \\ d_ik_{si} & 0 & b_ik_{si} \end{bmatrix} \tag{52}$$

where the k_{ji} parameters are defined using the p_i variable used before:

$$k_{1i} = (1-2p_i)c_1^{(1-2p_i)} \tag{53a}$$

$$k_{1i} = (1-2p_i)c_2^{(1-2p_i)} \tag{53b}$$

$$k_{1i} = (1-2p_i)c_s^{(1-2p_i)} \tag{53c}$$

The structure of Eq. 52 is considerably more complex than that of Eq. 49, where in the former we can appreciate a more extensive participation of elemental parameters such as interpolation function coefficients and functions that are domain dependent (interface location/orientation dependent) within nodal summations. No unconditional stability can be readily assured in Eq. 52.

While the specific subspace of parameters that drive $\mathbf{K}_{ww}$ unstable for the consistent enhancement will not be calculated in a rigorous fashion in this work, it is not hard to see that there is a condition that will intuitively introduce mathematical ambiguity problems: when the interface plane crosses exactly or very close to one or more element nodes, where it makes a sudden change of behaviour. If a given finite element model manages a non-structured mesh with random orientations while also having random material interfaces, instability or near-instability conditions will be certain to happen in some elements with a sufficiently large mesh. Implementation efforts have to consider this fact.

4.4. Stiffness matrices and impact to the global solution process

One of the most attractive features of the E-FEM framework is its ability to limit the work with field enhancements and all their associated variables within internal element calculation routines. All stiffness calculations derived from the special internal calculations associated to the discontinuities can be condensed and integrated to the standard elemental stiffness matrix. This way, no formal degrees of freedom are added to the finite element global solution process, so that the methods, routines and the solution platform shall remain untouched. However, the classical stiffness matrix properties normally identified in standard finite elements may change depending on the structure of the embedded enhancement.

For the weak discontinuity enhancements presented in this work, the numerical solution process and the construction of an *equivalent* stiffness matrix can be started by taking Eq. 7a (elemental force balance) and Eq. 17a (main relation between nodal displacements and weak discontinuity variables) to build the following linear system:

$$\mathbf{K}_{bb}\boldsymbol{d} + \mathbf{K}_{bw}[|\boldsymbol{\varepsilon}|] = \boldsymbol{f}^{e}_{ext} \tag{54a}$$

$$\mathbf{K}_{wb}\boldsymbol{d} + \mathbf{K}_{ww}[|\boldsymbol{\varepsilon}|] = \mathbf{0} \tag{54b}$$

Here, Eq. 7a has been integrated using the previously defined operators depending on the enhancement version to define stiffness matrices $\mathbf{K}_{bb}$ and $\mathbf{K}_{bw}$.

Condensation of the system then takes place by reducing $[|\boldsymbol{\varepsilon}|]$ from Eq. 54b and substituting on Eq. 54a, giving rise to a definition of an equivalent elemental stiffness matrix $\mathbf{K}_{sc}$ multiplying the standard normal displacements vector $\boldsymbol{d}$:

$$\mathbf{K}_{sc}\boldsymbol{d} = \boldsymbol{f}^{e}_{ext} \tag{55a}$$

$$\mathbf{K}_{sc} = \mathbf{K}_{bb} - \mathbf{K}_{bw}\mathbf{K}_{ww}^{-1}\mathbf{K}_{wb} \tag{55b}$$

With this, a global stiffness matrix assembly process may then be performed by taking the corresponding matrices $\mathbf{K}_{sc}$ associated to each element on a given model.

For the case of a typical weak discontinuity enhancement, it is not hard to see that:

$$\begin{aligned}\mathbf{K}_{bw} &= \tfrac{V^+V^-}{V}\mathbf{B}^T\left[\mathbf{C}^+ - \mathbf{C}^-\right]\mathbf{H}_w = \\ &\left\{\tfrac{V^+V^-}{V}\mathbf{H}_w^T\left[\mathbf{C}^+ - \mathbf{C}^-\right]\mathbf{B}\right\}^T = \mathbf{K}_{wb}^T\end{aligned} \tag{56}$$

so that:

$$\begin{aligned}&\left(\mathbf{K}_{bw}\mathbf{K}_{ww}^{-1}\mathbf{K}_{wb}\right)^T = \\ &\mathbf{K}_{wb}^T\left(\mathbf{K}_{ww}^{-1}\right)^T\mathbf{K}_{bw}^T = \mathbf{K}_{bw}\mathbf{K}_{ww}^{-1}\mathbf{K}_{wb}\end{aligned} \tag{57}$$

Given that $\mathbf{K}_{bb}$ is already symmetric, it can be concluded that the condensation process will always return a **symmetric** $\mathbf{K}_{sc}$. On the other hand, with the consistent enhancement, this is not the case:

$$\begin{aligned}&\left\{\mathbf{B}^T\sum_{i}^{N_e} C_{i,2}^{-1}\left[(1-p_i)V^+ + p_iV^-\right]\mathbf{C}\boldsymbol{H}_{w,i}\right\}^T \neq \\ &\tfrac{V^+V^-}{V}\mathbf{H}_w^T\left[\mathbf{C}^+ - \mathbf{C}^-\right]\mathbf{B}\end{aligned} \tag{58a}$$

$$\mathbf{K}_{bw} \neq \mathbf{K}_{wb}^T \tag{58b}$$

Indeed, the consistent enhancement will, *in general*, return an **asymmetrical** stiffness matrix. This will introduce the need to use asymmetric solvers during a global numerical solution, with all computational and implementation implications that come along.

4.5. Variational consistency errors in the typical enhancement

Now that it is known that the typical enhancement in general will not comply with basic requirement 3 (Eq. 11), it is relevant to discuss the conditions under which the formulation might produce large variational errors and the ones in which these errors will be kept within a reasonable range.

For a case of a 1-D element, like in the applications done by Benkemoun [34] or Melnyk [33], there can be only one node on each side of the material interface, and its orientation will always be normal to the line defining the body of the element. Under these conditions, it can be shown that the only difference between a typical and a consistent enhancement is only a constant offset $\Delta\tilde{u}$ on the displacement function (refer to Fig. 3). Given that the slopes coincide and the operators of the formulation are based on field derivatives, it can be concluded that the typical formulation effectively complies with requirement 3 and thus also remains fully variationally consistent.

For 2D and 3D elements in general, this is not the case. The slope of the typical enhancement will always be aligned to the orientation of the interface Γ_d. If more than one node is present on one of the domains, the enhancement will not be able to return the same field value on all nodes simultaneously, no matter what offset is given to the field. The only condition in which this might happen is when the nodes within a domain are all located on the same ξ coordinate, which would mean having element geometry aligned to the material interface. As the respective nodal ξ coordinates start to divert, the typical field will miss to nullify the values at the boundaries. Fig. 4 illustrates this for a 2D constant stress triangle (CST). The offset $\Delta\tilde{u}$ can be arranged to minimize this variational error by making the field to roughly pass through zero at an *average* ξ position of all nodes on a given domain.

Based on this rationale, the typical enhancement can be perceived as an *average estimation* of a fully consistent enhancement that will be closer to it under certain mesh geometry conditions. It can be expected that for an unstructured mesh with good aspect ratios, this estimation will grant reasonable results compared to a fully consistent approach. For a heavily distorted mesh having a very large disparity on ξ coordinates within a domain, the variational errors induced will certainly get larger.

5. Numerical simulations

In this section, a couple numerical simulation setups are presented to the reader to discuss on the performance of the different E-FEM enhancements with respect to an analytical solution reference as well as to a standard FEM model featuring an adapted mesh. First, a simple heterogeneous physical problem having an analytical solution is approached with a numerical model having a small number of elements. This will allow the reader to appreciate the behavior of the E-FEM formulations from a basic perspective, discussing on their ability to reproduce highly controlled and predictable mechanical fields as well as the sensitivity of the formulations' performance on mesh quality. Then, more complex numerical simulations will portray a more realistic heterogeneous sample by modelling a cubical matrix material domain having numerous regular inclusions of different sizes. A comparison will be made to a standard FEM setup having an adapted mesh to discuss on the overall comparative performance of the E-FEM enhancements depending on mesh sensitivity.

The reader can find another example of heterogeneous structure comparison simulations to test embedded weak discontinuity formulations in the works of Karavelic et al. [66] and Ibrahimbegovic et al. [67].

5.1. Bi-material layered model

The first set of simulations have been done on a simple cube model made up of two material layers separated by a planar interface. The interface is parallel to two of the cube faces. If interface

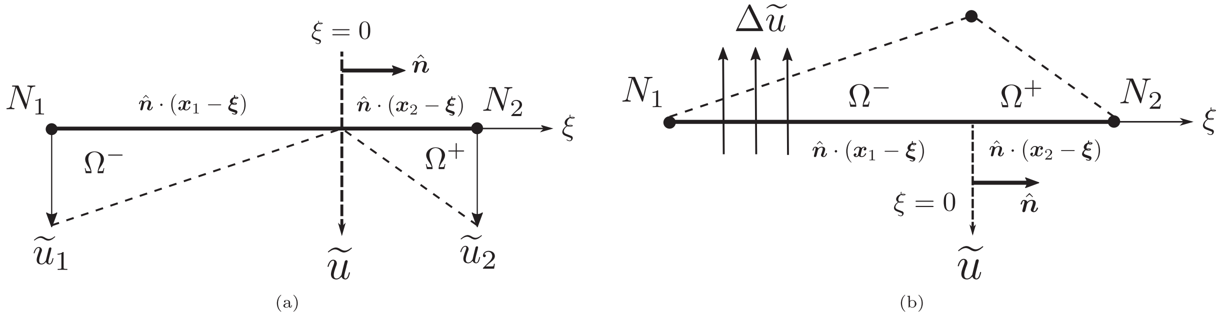

Fig. 3. Graphical analysis on 1D typical weak discontinuity enhancements. (a) Original enhanced field. (b) Enhanced field with an offset $\Delta\widetilde{u}$. Nullification of the field at element nodes can be achieved by adding an offset $\Delta\widetilde{u}$.

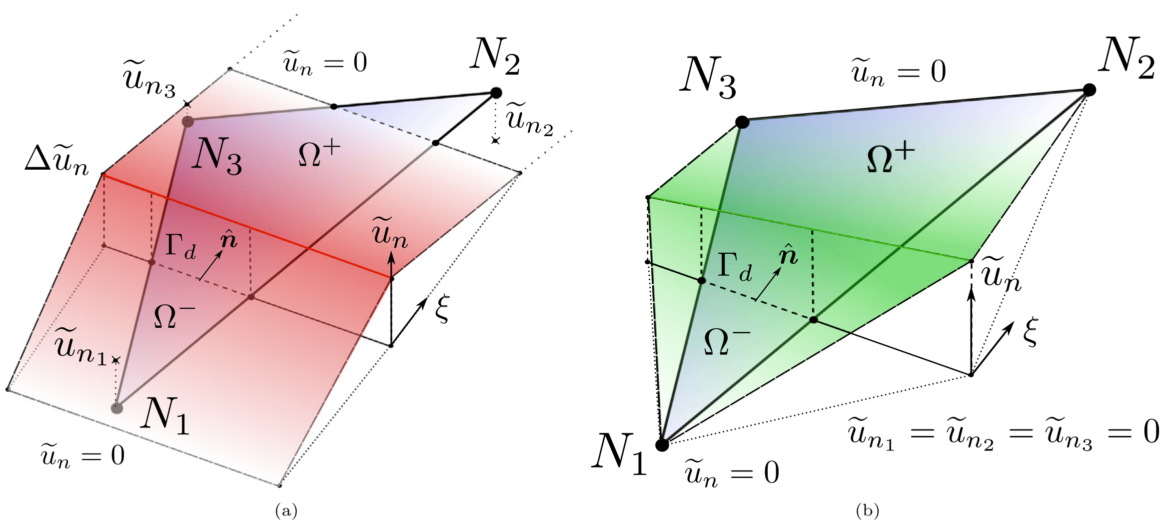

Fig. 4. Graphical analysis on 2D typical weak discontinuity enhancements taking a constant stress triangle (CST) as the base element, compared to a consistent enhancement. For the typical enhancement, it is assumed that an offset $\Delta\widetilde{u}_n$ has been given to the field to minimize the error when trying to nullify field values on the CST nodes. (a) Typical enhanced field over a CST. (b) Consistent enhanced field over a CST.

concentrations are neglected, the total axial reaction associated to a normal displacement on one of the faces can be calculated by means of the classical theory of mechanics of materials, representing the system as two springs in series accounting for the axial stiffness of each layer. Linear elastic behavior is assumed for both materials, characterized by Young Moduli E^+, E^- and Poisson ratios ν^+, ν^-. Fig. 5 illustrates this simple mechanical system.

The idea of the present study is to compare how each of the weak discontinuity enhancements can model this ideal bi-material layout by comparing them to the classical analytical solution. The interface plane location h will be varied taking regular steps from having a zero position at one of the cube faces until reaching the opposite side of the cube. This will represent situations in which the cube starts completely homogeneous with one of the material phases and gradually becomes entirely filled with the other material phase.

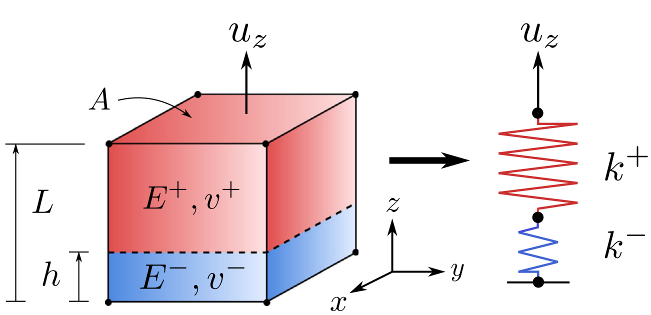

Fig. 5. Basic description of a bi-material layered prismatic body with total height L and cross section A, treated as a two-spring mechanical system in series having constants k^+ and k^-. The stiffness partition depends of the position h of the interface plane.

5.1.1. Numerical model

The cube will feature an unstructured mesh, totally independent from the planar interface. The interface will cross a certain amount of elements on random edges and positions, and these elements will be enhanced with one of the weak discontinuity field functions studied in previous sections. Special care has been taken with the mesh density in this study: the size of the elements should be small enough to generate enough enhanced elements, but these special elements should cover a significant amount of the cube volume in order to have a significant contribution to the global response of the model. This way, the influence of the E-FEM enhancements will be clearly perceived. If the elements are too small, we might get a large number of enhanced elements near the interface, but also a much larger amount of *normal* elements having only one material phase or the other, and thus the global stiffness response of the numerical sample will be dominated by the standard finite elements instead, which are not the object of this study. The mesh finally selected for this study is shown in Fig. 6, also highlighting the number of enhanced elements resulting from having the planar interface at 30% height from the designed bottom position. It is pertinent to mention that the quality of the mesh has been kept rather high, with no aspect ratios going beyond 3.

The cube has dimensions of $10\,\mathrm{mm} \times 10\,\mathrm{mm} \times 10\,\mathrm{mm}$. The material properties chosen for these simulations have been those normally associated to a simplified concrete mixture: a material phase of mortar (Young modulus $E^- = 14000\,\mathrm{MPa}$, Poisson ratio $\nu^- = 0.2$) and an aggregate material ($E^+ = 70000\,\mathrm{MPa}$, $\nu^+ = 0.2$). No other material properties are needed since all simulations have been made in static conditions. Boundary conditions have been set as to retain an ideal axial prism problem as much as possible without significant effects of near-interface field concentrations. The load has been imposed as a uniform displacement of $0.015\,\mathrm{mm}$ on the free upper face. Fig. 7 illustrates the details of the model.

FEAP (Finite Element Analysis Program) [68] has been used as the finite element numerical solution platform to implement both enhancements described in previous sections and for simulating the problem mentioned beforehand. 21 static-implicit simulations have been performed considering each weak discontinuity enhancement approach having 21 uniformly separated positions for the interface plane, going from the lower z face of the cube ($h = 0$) all the way to the opposite face ($h = 10\,\mathrm{mm}$) taking steps of 0.5 mm. The solution is strictly linear elastic, where the only solver-specific difference between each enhancement case has been the use of symmetric and asymmetric stiffness matrix handling routines, which are used only one time at the beginning of each analysis. Direct linear equation system solvers are used in either case.

Two different kinds of results have been considered for the current discussion in this work. One is the total vertical force reaction associated to the imposed displacement load for each case of interface plane position. The analytical calculation can be easily done attending to the representation in Fig. 5 and finding the total vertical reaction through an equivalent stiffness k_{eq}:

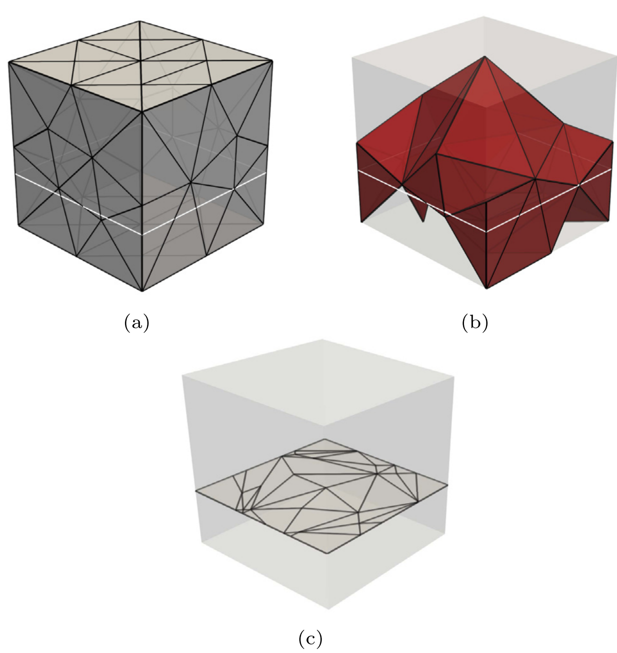

Fig. 6. General mesh description and view of all enriched elements crossed by the material interface plane. (a) General view of entire model mesh. Interface in white outline. (b) Mesh view isolating all enriched elements. Interface in white outline. (c) The discontinuity surfaces Γ_d for each element cut by the material interface. 92 elements and 43 nodes are used for the entire model. Enriched elements make up approximately for 50% of total volume.

$$F_z = u_z k_{eq} \tag{59a}$$

$$k_{eq} = \frac{k^+ k^-}{k^+ + k^-} \tag{59b}$$

$$k^{\pm} = \frac{SE^{\pm}}{L^{\pm}} \tag{59c}$$

The other output of interest is the average strain field value on each side of the interface. Analytically, these values are easily obtainable by just making:

$$\varepsilon^{\pm} = \frac{\sigma^{\pm}}{E^{\pm}} = \frac{F_z}{SE^{\pm}} \tag{60}$$

5.1.2. Vertical reaction analysis

Numerical simulation results coming from both enhancement types for the vertical force reaction can be appreciated in Fig. 8. This information is also shown as a relative error in Fig. 9. The first and last points in this plot represent the cases in which homogeneous material distributions are given for one or the other material phases (stiffer case and more compliant case, respectively), in which all numerical and analytical models naturally coincide. In the first part of the curves where the stiffer material is predominant, both weak discontinuity enhancements coincide for a while having a consistent error with respect to the analytical curve. At some point after having at least 20% volume fraction of the $(-)$ material region, the consistent enhancement error drops almost entirely, closely sticking to the analytical curve until the end of the graph. The typical enhancement maintains a smooth behavior with a consistent error, which also fades at the end when the $(-)$ material dominates completely. A maximum error of approximately 19% is observed with the typical enhancement. The sudden variations on the consistent enhancement can be explained by its natural stability conditions depending on node positions relative to the cutting plane interface, already discussed in Section 4.3.

As mentioned in the previous theoretical analysis section, it is also the interest of the authors to address the importance of the effect of mesh quality on the difference of performance between the typical and the consistent enhancements. For this, mesh presented in Fig. 6a has been deliberately distorted by pushing the nodes above the material interface plane position up and the remaining nodes down. This way, the same enhanced elements remain crossed by the interface as in the base scenario, and any change in results is directly attributable to the change in shape quality of these elements. The average aspect ratio of the affected elements has been set as the main sensitivity metric for this study. For the tetrahedral elements managed in all these simulations, the aspect ratio mesh metric is defined as follows:

$$Q = \frac{h_{max}}{2\sqrt{6}r} \tag{61}$$

where h_{max} is the maximum edge length of the tetrahedron and r is the radius of the inscribed sphere within it. Q can take values from 1.0 for a perfectly regular tetrahedron and grow up indefinitely for distorted shapes. Fig. 10 shows the case where the distortion method proposed produces a mesh with an average aspect ratio of 1.92 and other with 3.55. This metric has been varied from 1.82 to 5.05 taking ten different values. The position of the interface has been fixed at h = 3 mm as this has been identified as a data point that shows a prominent performance sensitivity between the typical and the consistent enhancements. The idea is to show the evolution of the prediction errors for the global vertical reaction as the average aspect ratio increases, in order to study how each of the formulations is able to remain robust to mesh quality variations.

Fig. 11 shows the overall results of the evolution of the prediction error with respect to an increase in average aspect ratios.

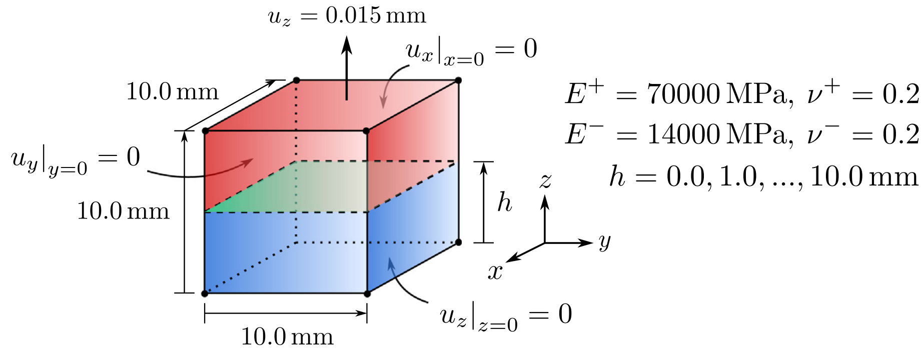

Fig. 7. Description of model details, as simulated in the FEAP program.

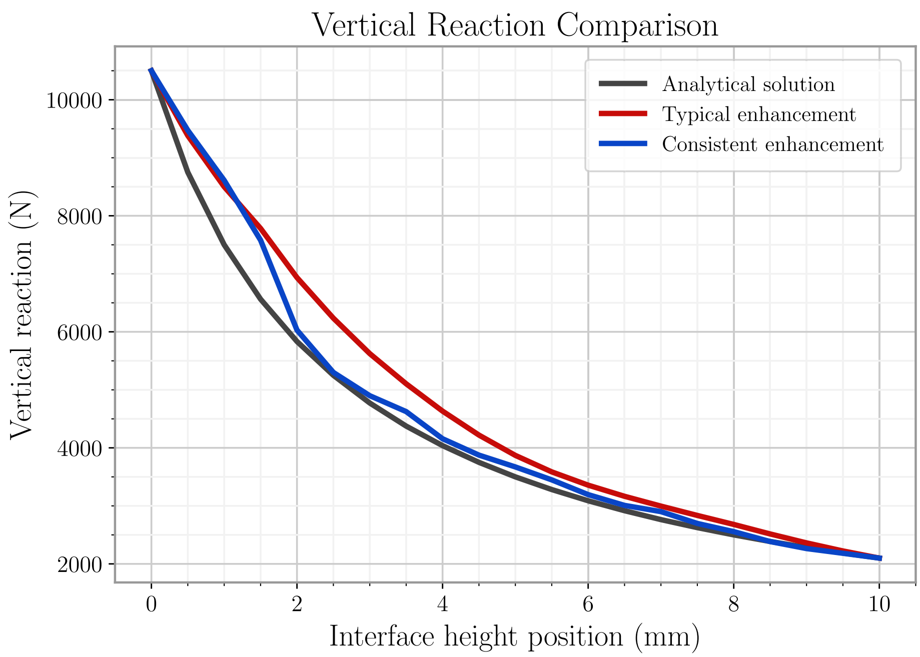

Fig. 8. Vertical reaction on the entire lower face of the cube model for both enhancement types and the analytical solution.

Regardless of the fact that the typical enhancement already started with a higher prediction error than the consistent E-FEM enhancement, results suggest that the typical enhancement consistently increases its prediction error as the elements get more distorted, starting from 19% and reaching up to a 27% error. The consistent enhancement seems to follow the same trend momentarily, only to fall once again back to its beginning error level of 4% and steadily remains there. Even if the distortion method proposed does not allow to get to very high aspect ratios in this study, the results support the hypothesis introduced in Section 4.5, favoring once again, the asymmetrical robustness of the fully consistent E-FEM enhancement.

Finally, simulations were done to assess the sensitivity of the formulations to the difference in material properties between the two phases. The ratio of Young moduli (E^+/E^-) was considered as the metric in this case. The same position for the interface place as with the previous mesh quality study was fixed, and the ratio between elastic moduli was varied from 5 (original case) up to 50. The evolution of the vertical reaction prediction error is plotted for both formulations in Fig. 12. This is considered by the authors of this work as the most sensitive parameter so far concerning formulation performance, driving the error of the typical E-FEM enhancement as high as 80%, while the consistent formulation remains within the 10% threshold.

5.1.3. Strain field analysis

The displacement load imposed to this simple model will ideally produce a piece-wise, constant strain field. The numerical approaches should be able to produce these constant strain regions taking the contribution of all elements on each side of the interface, aiming to have the least dispersion as possible. For this, the *average* strain field and its *dispersion* (standard deviation) have been calculated on each side of the cube model interface for both enhancement approaches, and results have been compared to the analytical model. The analytical results, of course, do not show any kind of field dispersion as they only exhibit a unique strain value. Fig. 13 shows this comparison for the case of the (+) material side. Again, at homogeneous conditions all models coincide. Both enhancements start diverging at the beginning and the consistent enhancement quickly catches up the analytical behavior with a mild error. The typical enhancement, once again, has a smoother curve keeping a sustained error. The last data point at $h = 10$ mm is not shown since the (+) region ceases to exist. The strain dispersion, represented as a translucent cloud around each enhancement curve, seems definitely more controlled for the consistent enhancement, albeit with apparently more erratic fluctuations coming from the stability nature of this formulation.

Fig. 14 shows the analysis on the remaining material region. In this case, it is the first point at zero that is missing since there is no

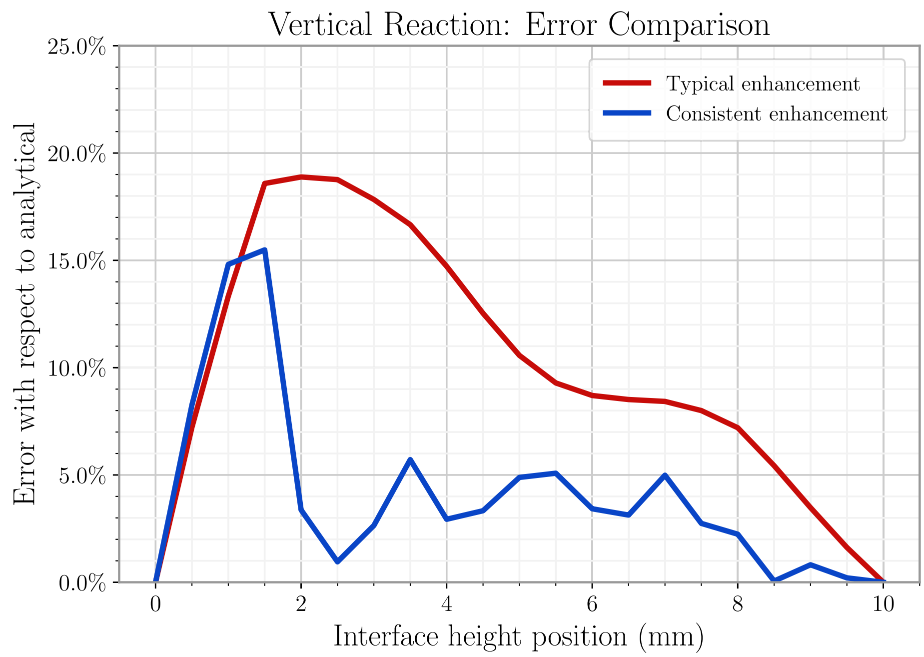

Fig. 9. Vertical reaction comparison between the typical and full consistent weak discontinuity formulations in a relative error format.

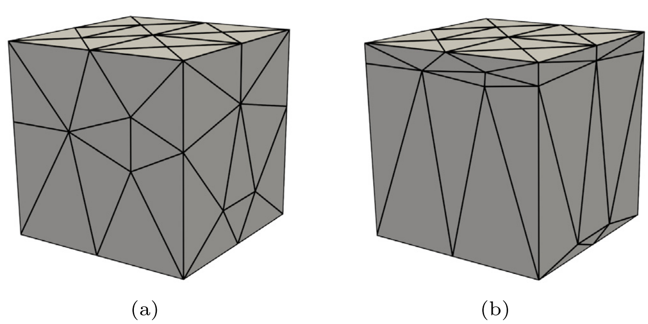

Fig. 10. Two of the distorted mesh configurations taken for assessing mesh quality sensitivity: (a) Base mesh with a distortion yielding an average aspect ratio of 1.92 (b) Base mesh with a distortion yielding an average aspect ratio of 3.55.

$(-)$ material. The average strain again favours the consistent enhancement that keeps a lower error through all conditions. The dispersion of the consistent model is also remarkably low, with the exception of one point at 30% volume for the $(-)$ material, where an outlier data point occurs. After model inspections, it is indeed found that at this height many nodes lie very close to the interface with separations as low as 0.03 mm, which seemingly compromise the stability of this enhancement as discussed in Section 4.3. The impact of this outlier is not noticeable for the case of the analysis on the $(+)$ domain, since at $h = 3$ mm there are considerably more homogeneous elements made up of the $(+)$ material, which help to smooth these statistics.

5.2. Heterogeneous model with regular inclusions

The last set of simulations feature a more realistic representation of a heterogeneous material sample. It consists of a cubical homogeneous material matrix ($10\,\text{mm} \times 10\,\text{mm} \times 10\,\text{mm}$), having spherical inclusions of different sizes, varying from 0.5 mm to 2.0 mm. This morphology was obtained using a random spherical inclusion generator included on the SPAM Python library [69]. Fig. 15 shows a translucent image of it revealing the distribution of the inclusions, as well as a cross section corresponding to the center vertical plane (YZ).

Two different meshing methods were used for building the models of the current study: adapted and non-adapted. The adapted mesh is meant to be used by a standard FEM approach. A target characteristic size is set by using the Gmsh library [70], and the mesh is forced to respect absolutely all boundaries between the matrix and the inclusions. With such conditions, the meshing engine will not be able to always respect the size target value, specially at the inclusion interfaces, but will try to keep up with the requested size whenever possible. No local refinement techniques are used for this morphology. The mesh in this adapted model is refined by the mere action of reducing the target characteristic mesh size. Fig. 16 shows the central cross section (YZ) for a characteristic size target of 1.0 mm and 0.35 mm.

The non-adapted mesh is used for the two E-FEM formulations already described in this work. A completely unstructured and regular tetrahedral mesh is built for a given mesh characteristic size, with no regard with respect to the morphology of the inclusions. The morphology distribution is then projected onto the mesh using the particular E-FEM inputs discussed earlier for each element falling within an interface. This procedure is also performed by the SPAM library. For a given size, the same mesh is used for both typical and consistent E-FEM formulations.

For both adapted and non-adapted mesh types, different mesh setups were produced going from a characteristic size of 1.5 mm down to 0.1 mm, yielding element counts from the order of 2×10^3 to 3×10^6 elements, respectively. For the case of the fully consistent E-FEM enhancement, simulations were done until reaching the characteristic size of 0.35 mm (roughly 100 k elements) due to the asymmetrical tangent matrix solution limitations using the FEAP solver engine and the given computational resources used for these simulations. After analysing the results, the authors of this work have deemed this still sufficient enough to draw meaningful conclusions on the fully consistent E-FEM formulation.

As a loading scheme, the same vertical tensile displacement has been exerted all simulation setups as already seen in the previous section. All simulations remain on the linear elastic regime, and the same material properties used for the previous simulation were

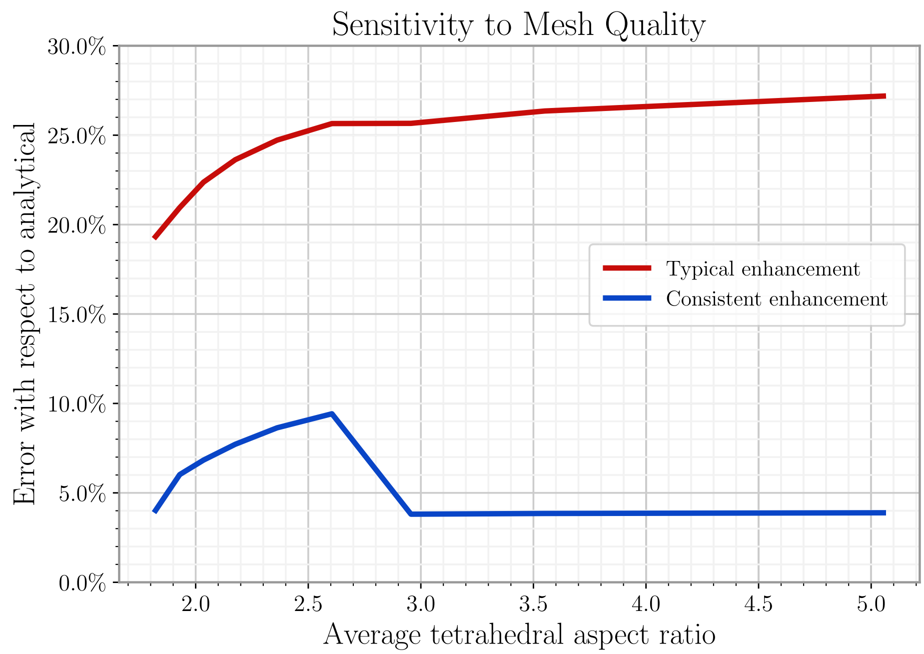

Fig. 11. Vertical reaction error dependency on mesh quality through the average aspect ratio of elements involved in the material interface. The interface has been fixed at 30% of the cube height in these simulations.

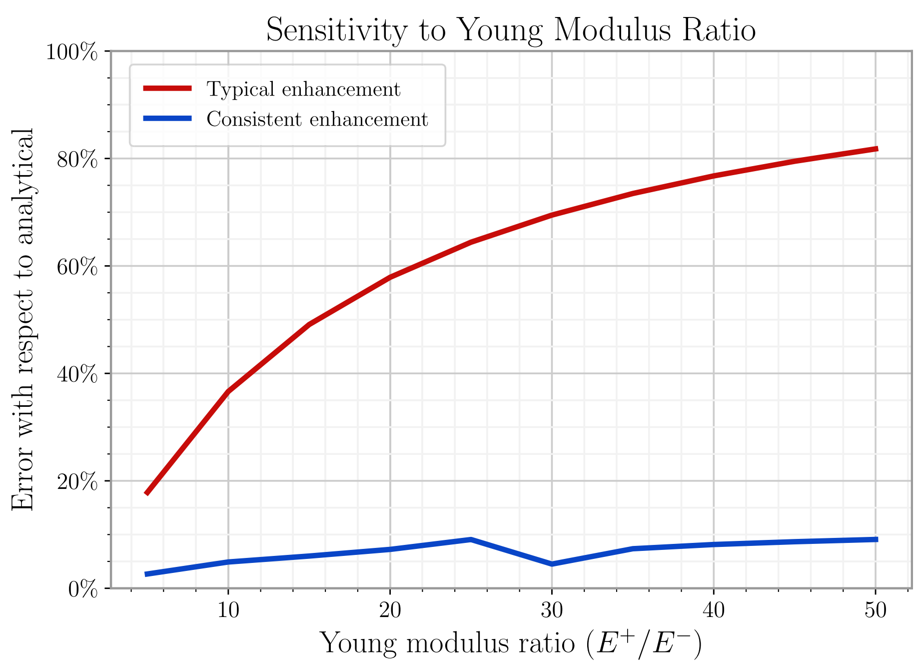

Fig. 12. Vertical reaction error dependency on the Young moduli ratio E^+/E^- between both material domains. The interface has been fixed at 30% of the cube height in these simulations.

used. This way, the model is now more representative of a concrete sample.

5.2.1. Response sensitivity analysis

A first mesh sensitivity study is done on the adapted mesh model with the standard FEM taking two global mechanical outputs: the vertical reaction and a metric describing the stored elastic energy E_{int} on all the surfaces of all the inclusions in the model. The latter has been defined as an integrated scalar field through all the tetrahedron faces falling directly on the inclusion interface locations:

$$E_{int} = \sum_{i}^{N_{inc}} \int \overline{\boldsymbol{\sigma}} : \overline{\boldsymbol{\varepsilon}} \, dA \approx \sum_{i}^{N_{inc}} \sum_{j}^{N_e} \overline{\boldsymbol{\sigma}_j} : \overline{\boldsymbol{\varepsilon}_j} A_j \tag{62}$$

where N_{inc} is the number of inclusions, N_e the number of element faces associated to each interface, A_j the area of each of such faces and $\overline{\boldsymbol{\sigma}}_j, \overline{\boldsymbol{\varepsilon}}_j$ are estimated interface strain and interface stress tensors, calculated as:

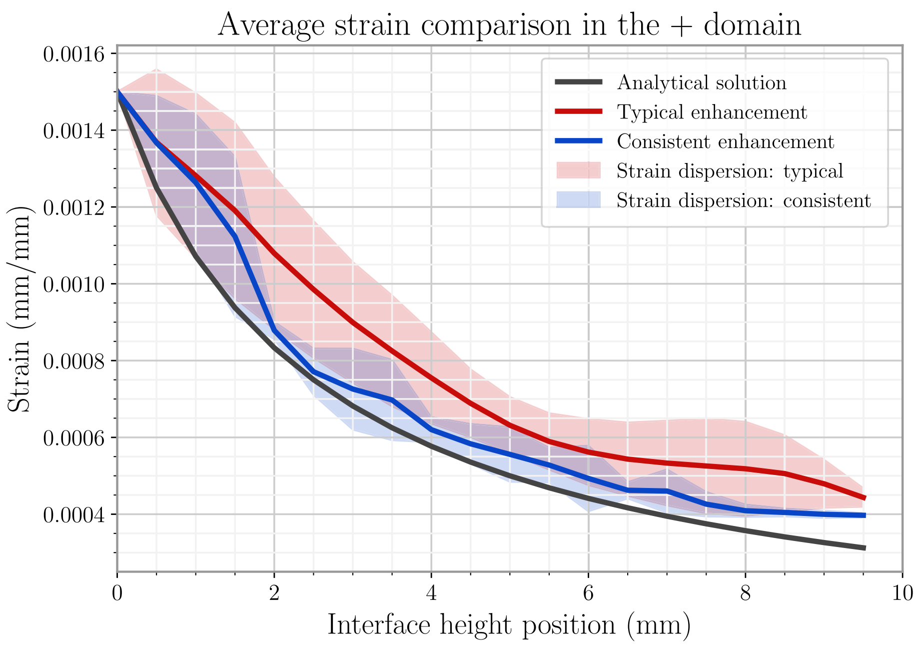

Fig. 13. Average strain and corresponding dispersion for both weak discontinuity enhancements compared to analytical calculations on the (+) (stiffer material) domain.

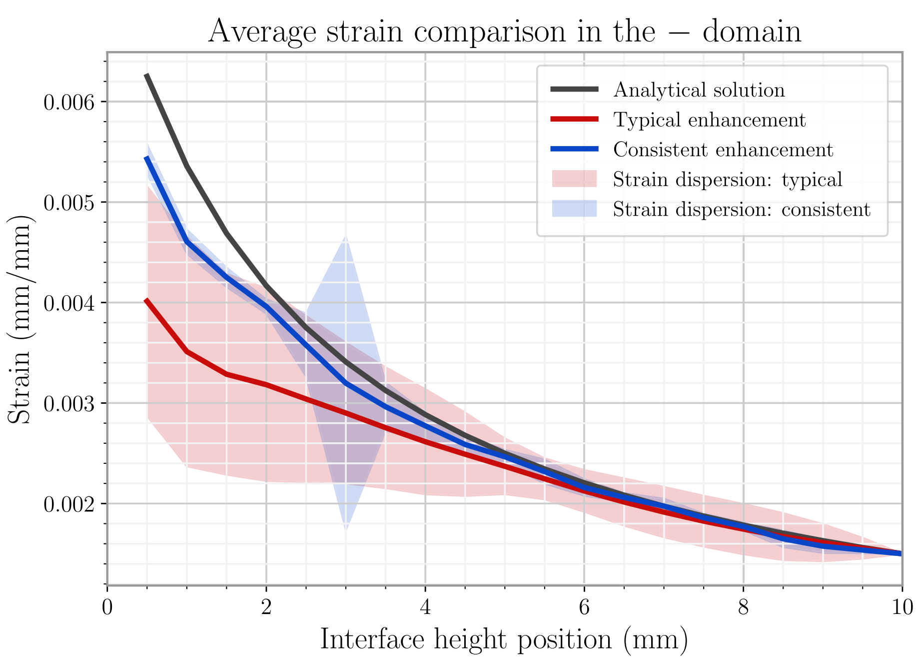

Fig. 14. Average strain and corresponding dispersion for both weak discontinuity enhancements compared to analytical calculations on the (−) (more compliant) domain.

$$\overline{\boldsymbol{\sigma}_j} = \frac{V_j^+ \boldsymbol{\sigma}_j^+ + V_j^- \boldsymbol{\sigma}_j^-}{V_j^+ + V_j^-}; \quad \overline{\boldsymbol{\varepsilon}_j} = \frac{V_j^+ \boldsymbol{\varepsilon}_j^+ + V_j^- \boldsymbol{\varepsilon}_j^-}{V_j^+ + V_j^-} \tag{63}$$

where the weighting volumes V_j^+, V_j^- are those associated to the elements on each side of the triangular face on the interface. The double dot product $\overline{\boldsymbol{\sigma}_j} : \overline{\boldsymbol{\varepsilon}_j}$ yields an energy density per volume, and thus the integrals of Eq. 62 yield a normalized energy by thickness. This metric is meant to provide with a global mechanical output that is able to summarize a general state of all material interfaces of the inclusions at once, which is one of the main interests when performing simulations of heterogeneous material samples.

Both reaction and interface energy global outputs are extracted from successive simulations with the adapted mesh model having the mesh characteristic size decreased down to a point where both metrics stabilise. These final values are taken as the global output reference to which the E-FEM simulation results will be compared. For the case of this specific model, the vertical reaction stabilises at approximately 930.5 N, while the interface energy metric stabilises at 2.1 J/m. By taking these references, the authors of this work are making the assumption that a sufficiently refined adapted mesh model using the standard FEM approach will return a physically accurate mechanical response.

For the non-adapted meshes, the E-FEM routines naturally calculate $\overline{\boldsymbol{\sigma}_j} : \overline{\boldsymbol{\varepsilon}_j}$ by taking the subvolumes of each of the segmented elements as the weighting factors, which remains consistent with

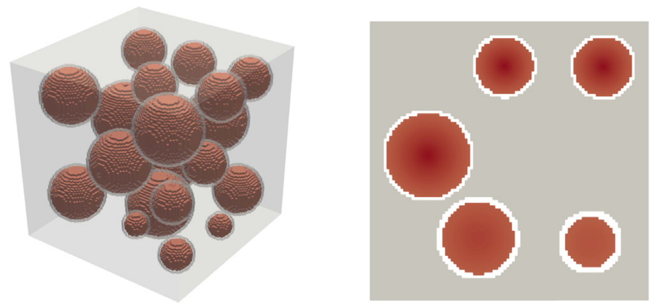

(a) (b)

Fig. 15. Display of the heterogeneous morphology with a uniform matrix and multiple regular inclusions: (a) Transparent matrix material (b) Mid-plane slice view with interfaces highlighted. These images have been extracted from a distance field output produced by the SPAM library.

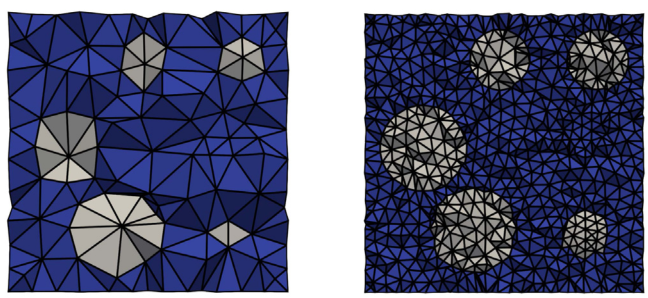

(a) (b)

Fig. 16. Mid-plane slice views of the adapted mesh built for the heterogeneous morphology: (a) having a characteristic goal size of 1.0 mm (b) having a characteristic goal size of 0.35 mm.

Eq. 63. The area A_j in this case is calculated taking the surface of the local interface within the element in this case.

Figs. 18 and 17 show the comparative results of the standard FEM results with respect to both typical and fully consistent E-FEM models. These results are normalized with respect to each of the global output references, so that a value of 1.0 denotes the stable goal value aimed by all models. For the case of the vertical reaction, it is observed that both E-FEM models are able to approach very close to the goal stable value. The remarkable trait of this analysis is that the fully consistent E-FEM enhancement is able to deliver a response practically on the reference goal with an element count as low as 30 k elements. The adapted model requires an overall refined model with at least 2 million elements to reach this same level of stable response. The typical E-FEM model has a slightly inferior performance, always keeping in mind that its response remains still very accurate overall (1% error). The analysis on the energy metric seems to magnify this tendency. All models begin with a poor prediction of the stable value for then reaching a relatively stable bound, which does not reach the stable reference for the case of both E-FEM models. Again, the fully consistent E-FEM formulation seems to achieve the highest fidelity with respect to the reference goal, and it does so with a very reduced number of elements (20 k). The adapted model requires, once again, a considerable level of refinement in order to make up for the lack of multiphasic representation power with at least one million elements overall.

6. Conclusions

A detailed analysis has been made on the use of weak discontinuity approaches within the E-FEM framework to model material heterogeneities. Kinematic and variational theoretical bases have been stated to identify a set of consistency requirements for the general construction of weak discontinuity displacement enhancement fields. Based on the consideration of these requirements, two field proposals have been derived: one which has been already used in the works of Roubin, Hauseux and Stamati [22,63,55], and other which is fully consistent with all variational requirements.

Simulations have been made on a simple bi-material system subjected to an axial load to assess the performance of the enhancements with a basic model where the enhanced elements represent a large amount of the sample space to amplify the effects

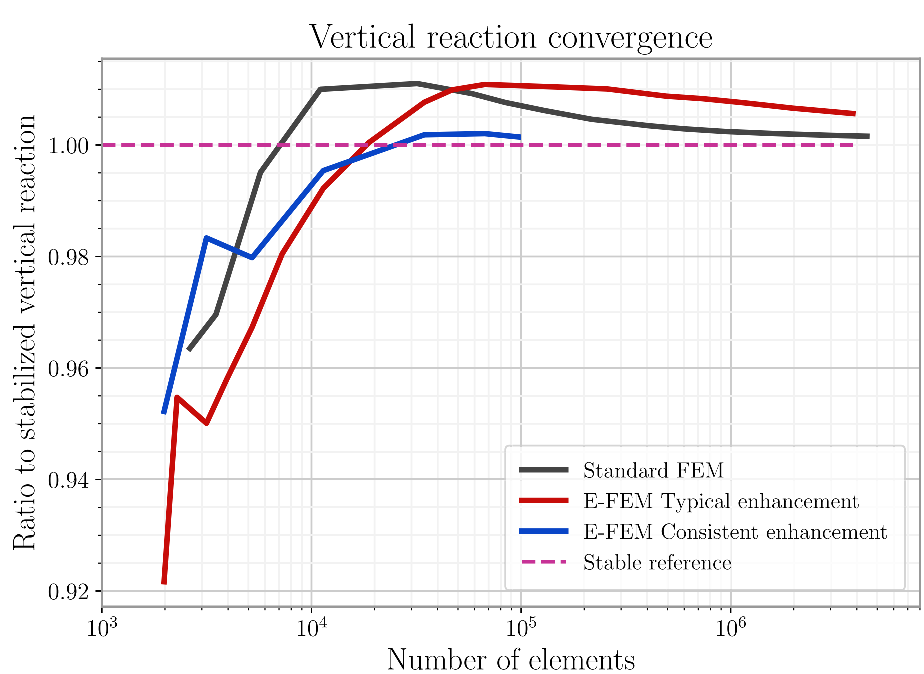

Fig. 17. Normalized vertical reaction behavior with respect to the amount of 3D elements in the model. A value of 1 corresponds to the stable reference fixed after a previous mesh sensitivity analysis with the standard FEM model having an adapted mesh.

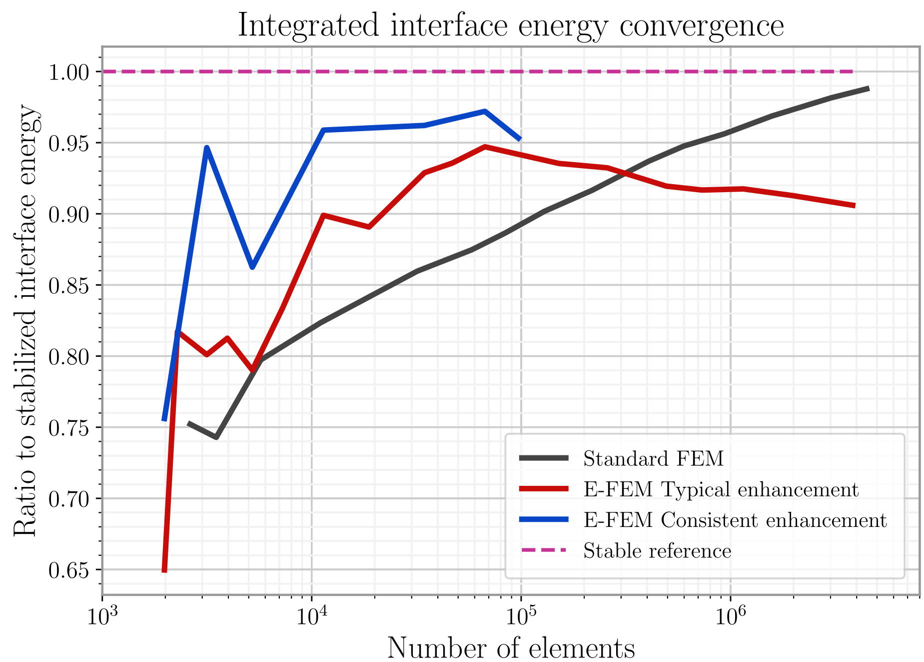

Fig. 18. Normalized energy metric behavior with respect to the amount of 3D elements in the model. A value of 1 corresponds to the stable reference fixed after a previous mesh sensitivity analysis with the standard FEM model having an adapted mesh.

of the enhancements on the global response. It has been seen that, in general, the consistent enhancement has a better performance than the typical enhancement at capturing an analytical global vertical reaction, but is more prone to uncontrolled fluctuations. The analysis was also done considering different mesh quality scenarios, where the average aspect ratio of the enhanced elements was varied. It has been observed that the typical enhancement consistently loses accuracy on its prediction with larger aspect ratios, while the fully consistent enhancement manages to retain its correlation level. This was already expected when comparing the characteristics of both enhancements in Section 4.5. A sensitivity analysis on material difference properties between the phases evidences what is considered by the authors the weakest point of the typical enhancement, where its prediction errors increased up to 80% as the ratio between elastic moduli went up to 50. This error is not acceptable and should carefully reconsider the use of the typical E-FEM enhancement to attempt any simulations of heterogeneous materials where there is a strong difference between elastic properties between material phases.

Further simulations in a more complex system depicting a heterogeneous concrete sample with a number of inclusions were done in order to assess the overall mesh sensitivity and to further compare the E-FEM-based models to a standard FEM setup having a completely adapted mesh respecting all the inclusion boundaries in a more realistic model setup. The reference of two different global output metrics were set based on a first sensitivity analysis done on the adapted mesh model until reaching their convergence. These were defined as the global vertical reaction and an integrated interface energy metric, where the latter attempts to capture a general mechanical state of all the inclusions in the domain. After comparing with the results coming from the E-FEM models, it was observed that both E-FEM models are able to reach the reference goal up to a certain threshold, having the best results with the fully consistent E-FEM formulation with less than 5% error in the case of the energy metric and less than 1% for the global reaction. It has been also found that, for this formulation, such levels of prediction are reached with a remarkably less number of elements than with the standard adapted mesh model, having a ratio of 20 k to 1 million elements to reach the same prediction level, respectively. These comparisons have taken the number of elements as the base model size unit since the E-FEM models are less sensitive to global DOF counts (the condensation approach is strictly local). The adapted mesh model could have benefited from a localised mesh refinement technique to be more efficient in terms of morphology representation, but the authors of this work also think that the E-FEM models can also benefit from such techniques in a similar way.

The benefits of developing a fully consistent E-FEM weak discontinuity formulation have been shown through these results. However, given its numerically asymmetrical nature, its use may find a better niche on problems where high accuracy is required for field shape calculations and where the use of an asymmetric solver poses no problem for a given FEM numerical solution platform. An scenario where the heterogeneous domain involves materials with a drastic difference in material properties will also drive a prominent need for a fully consistent E-FEM formulation. In any case, under high quality mesh conditions and a moderate difference between the elastic properties of material phases, the typical enhancement will have a reasonable behavior that will allow for sound estimations at local and global level mechanical outputs. The formulation by itself naturally presents unconditional stability and retains the symmetry of global stiffness matrices. The internal calculations required to particularise the function parameters are also considerably simpler than in the case of the consistent enhancement version. For these reasons, the authors of this study recommend its use whenever possible, especially when dealing with large and complex numerical models where solution times and stability are crucial for the success of the numerical analysis project.

In either case, the authors of this work finish by stating that the use of weak discontinuity enhancements for the representation of material heterogeneities remains a reliable and efficient numerical method for approaching the problem of multiple material phases representation featuring non-adapted meshes.

Declaration of Competing Interest

The authors declare that they have no known competing financial interests or personal relationships that could have appeared to influence the work reported in this paper.

References

[1] Rémond Y, Ahzi S, Baniassadi M, Garmestani H. Homogenization of Reconstructed RVE. John Wiley & Sons Ltd; 2016. p. 133–68. https://doi.org/10.1002/9781119307563.ch6.
[2] Weinan E. Principles of Multiscale Modeling. Cambridge: Cambridge University Press; 2011.
[3] You Y, Kou X, Tan S. Adaptive meshing for finite element analysis of heterogeneous materials. Comput Aided Des 2015;62:176–89.
[4] Favino M, Hunziker J, Caspari E, Quintal B, Holliger K, Krause R. Fully-automated adaptive mesh refinement for media embedding complex heterogeneities: application to poroelastic fluid pressure diffusion. Comput Geosci 2020;24.
[5] Efendiev Y, Kronsbein C, Legoll F. Multilevel Monte Carlo approaches for numerical homogenization. Multiscale Model Simul: A SIAM Interdiscip J 2015;13:1107–35.
[6] Nikolic M, Karavelić E, Ibrahimbegovic A, Miščević P. Lattice element models and their peculiarities. Arch Comput Methods Eng 2018;25:753–84.
[7] Xu T, Fu T-F, Heap M, Meredith P, Mitchell T, Baud P. Mesoscopic damage and fracturing of heterogeneous brittle rocks based on three-dimensional polycrystalline discrete element method. Rock Mech Rock Eng 2020;53.
[8] Shiu W, Donze F-V, Daudeville L. Compaction process in concrete during missile impact: a DEM analysis, Computers and Concrete, an. Int J 2008;5:329–42.
[9] Huang J, Chen M, Sun J. Mesoscopic characterization and modeling of microcracking in cementitious materials by the extended finite element method. Theoret Appl Mech Lett 2014;4:041001.
[10] Vandoren B, De Proft K, Simone A, Sluys L. Mesoscopic modelling of masonry using weak and strong discontinuities. Comput Methods Appl Mech Eng 2013;255:167–82.
[11] Diwan G, Mohamed MS, Seaid M, Trevelyan J, Laghrouche O. Mixed enrichment for the finite element method in heterogeneous media. Int J Numer Meth Eng 2015.
[12] Strouboulis T, Copps K, Babuška I. The generalized finite element method. Comput Methods Appl Mech Eng 2001;190:4081–193.
[13] Aragón AM, Duarte CA, Geubelle PH. Generalized finite element enrichment functions for discontinuous gradient fields. Int J Numer Meth Eng 2010;82:242–68.
[14] Li H, O'Hara P, Duarte C. Non-intrusive coupling of a 3-d generalized finite element method and abaqus for the multiscale analysis of localized defects and structural features. Finite Elem. Anal. Des. 2021;193:103554.
[15] Belytschko T, Parimi C, Moës N, Sukumar N, Usui S. Structured extended finite element methods for solids defined by implicit surfaces. Int. J. Numer. Meth. Eng. 2003;56:609–35.
[16] Belytschko T, Gracie R, Ventura G. A review of extended/generalized finite element methods for material modelling. Modell Simul Mater Sci Eng 2009;17:043001.
[17] Wu L, Zhang L, Guo Y. A review of the extended finite element for fracture analysis of structures. Appl Mech Mater 2013;444–445:96–102.
[18] Peng Y, Liu Y. Advances in the Base Force Element Method. Springer; 2019. https://doi.org/10.1007/978-981-13-5776-3.
[19] Peng Y, Chen X, Ying L, Chen Y, Zhang L. Mesoscopic numerical simulation of fracture process and failure mechanism of concrete based on convex aggregate model. Adv Mater Sci Eng 2019;2019:1–17.
[20] Jirásek M. Comparative study on finite elements with embedded cracks, Comput. Methods in Appl. Mech Eng 2000;188:307–30.
[21] Oliver J. Modelling strong discontinuities in solid mechanics via strain softening constitutive equations. part 1: fundamentals. Int J Numer Methods Eng. 1996;39:3575–600.
[22] Roubin E, Vallade A, Benkemoun N, Colliat J-B. Multi-scale failure of heterogeneous materials: A double kinematics enhancement for embedded finite element method. Int J Solids Struct 2015;52:180–96.
[23] Rabczuk T, Bordas S, Zi G. A three-dimensional meshfree method for continuous multiple-crack initiation, propagation and junction in statics and dynamics. Comput Mech 2007;40:473–95.
[24] Rabczuk T, Zi G, Bordas S, Nguyen-Xuan H. A simple and robust three-dimensional cracking-particle method without enrichment. Comput Methods Appl Mech Eng 2010;199:2437–55.
[25] Bordas S, Rabczuk T, Zi G. Three-dimensional crack initiation, propagation, branching and junction in non-linear materials by an extended meshfree method without asymptotic enrichment. Eng. Fract. Mech. 2008;75:943–60.
[26] Farina S, Claus S, Hale J, Skupin A, Bordas S. A cut finite element method for spatially resolved energy metabolism models in complex neuro-cell morphologies with minimal remeshing. Advanced Modeling and Simulation in Engineering Sciences 2021;8.
[27] Agathos K, Chatzi E, Bordas SP. Stable 3d extended finite elements with higher order enrichment for accurate non planar fracture. Comput Methods Appl Mech Eng 2016;306:19–46.
[28] An adapted deflated conjugate gradient solver for robust extended/generalised finite element solutions of large scale, 3d crack propagation problems, Computer Methods in Applied Mechanics and Engineering 395 (2022) 114937.
[29] Agathos K, Tatsis K, Nicoli S, Bordas SP, Chatzi E. Crack detection in mindlin-reissner plates under dynamic loads based on fusion of data and models. Computers & Structures 2021;246:106475.
[30] Agathos K, Chatzi E, Bordas SPA, Talaslidis D. A well-conditioned and optimally convergent xfem for 3d linear elastic fracture. Int J Numer Meth Eng 2016;105:643–77.
[31] Agathos K, Bordas SP, Chatzi E. Improving the conditioning of xfem/gfem for fracture mechanics problems through enrichment quasi-orthogonalization. Comput Methods Appl Mech Eng 2019;346:1051–73.
[32] Ibrahimbegovic A, Wilson EL. A modified method of incompatible modes. Communications in Applied Numerical Methods 1991;7:187–94.
[33] Ibrahimbegovic A, Melnyk S. Embedded discontinuity finite element method for modeling of localized failure in heterogeneous materials with structured mesh: An alternative to extended finite element method. Comput. Mech. 2007;40:149–55.
[34] Benkemoun N, Hautefeuille M, Colliat J-B, Ibrahimbegovic A. Failure of heterogeneous materials: 3d meso-scale fe models with embedded discontinuities. Int J Numer Meth Eng 2010;82:1671–88.
[35] Oliver J, Huespe A, Sánchez P. A comparative study on finite elements for capturing strong discontinuities: E-fem vs x-fem, Comput. Methods in Appl. Mech. Eng. 2006;195:4732–52.
[36] Stanic A, Brank B, Brancherie D. Fracture of quasi-brittle solids by continuum and discrete-crack damage models and embedded discontinuity formulation. Eng. Fract. Mech. 2020;227:106924.
[37] Ortiz M, Leroy Y, Needleman A. A finite element method for localized failure analysis. Comput Methods Appl Mech Eng 1987;61:189–214.
[38] Belytschko T, Fish J, Engelmann BE. A finite element with embedded localization zones. Comput Methods Appl Mech Eng 1988;70:59–89.
[39] Sluys L, Berends A. Discontinuous failure analysis for mode-i and mode-ii localization problems. Int. J. Solids Struct. 1998;35:4257–74.
[40] Larsson R, Runesson K, Sture S. Embedded localization band in undrained soil based on regularized strong discontinuity—theory and fe-analysis. Int. J. Solids Struct. 1996;33:3081–101.
[41] Simo JC, Oliver J, Armero F. An analysis of strong discontinuities induced by strain-softening in rate-independent inelastic solids. Comput. Mech. 1993;12:277–96.
[42] Oliver J. Modelling strong discontinuities in solid mechanics via strain softening constitutive equations. part 2: numerical simulation. Int J Numer Methods Eng. 1996;39:3601–23.
[43] Borja RI. A finite element model for strain localization analysis of strongly discontinuous fields based on standard galerkin approximation. Comput Methods Appl Mech Eng 2000;190:1529–49.
[44] Borst R, Wells G, Sluys L. Some observations on embedded discontinuity models, Engineering Computations: Int J for. Computer-Aided Engineering 2001;18:241–54.
[45] da Costa DD, Alfaiate J, Sluys L, Júlio E. A discrete strong discontinuity approach. Eng. Fract. Mech. 2009;76:1176–201.
[46] Jin T, Mourad H, Bronkhorst C, Livescu V. Finite element formulation with embedded weak discontinuities for strain localization under dynamic conditions. Comput. Mech. 2018;61:1–16.
[47] Jin T, Mourad HM, Bronkhorst CA, Livescu V, Zhang X, Linder C, Regueiro RA. Three-dimensional explicit finite element formulation for shear localization with global tracking of embedded weak discontinuities. Comput Methods Appl Mech Eng 2019;353:416–47.
[48] Linder C, Armero F. Finite elements with embedded strong discontinuities for the modeling of failure in solids. Int J Numer Methods Eng. 2007;72:1391–433.
[49] Alfaiate J, Simone A, Sluys L. Non-homogeneous displacement jumps in strong embedded discontinuities. Int J Solids Struct. 2003;40:5799–817.
[50] Sukumar N, Chopp D, Moës N, Belytschko T. Modeling holes and inclusions by level sets in the extended finite-element method. Comput Methods Appl Mech Eng 2001;190:6183–200.
[51] Markovic D, Niekamp R, Ibrahimbegovic A, Matthies H, Taylor R. Multi-scale modeling of heterogeneous structures with inelastic constitutive behaviour: Part i - physical and mathematical aspects, Engineering Computations: Int J for. Computer-Aided Engineering 2005;22:664–83.
[52] D. Markovic, Modélisation multi-échelles de structures hétérogènes aux comportements anélastiques non-linéaires, Theses, École normale supérieure de Cachan - ENS Cachan, Gif-sur-Yvette, France, 2004, 2004. URL: https://tel.archives-ouvertes.fr/tel-00133643.
[53] Hauseux P, Roubin E, Seyedi D, Colliat J-B. Fe modelling with strong discontinuities for 3d tensile and shear fractures: Application to underground excavation. Comput Methods Appl Mech Eng 2016;309.
[54] A. Vallade, Modélisation multi-échelles des shales: influence de la microstructure sur les propriétés macroscopiques et le processus de fracturation, Ph.D. thesis, Université de Lille [2015-....], Lille, France, 2016, 2016. URL: https://ori-nuxeo.univ-lille1.fr/nuxeo/site/esupversions/c532cf32-5811-4435-a780-20ebef3f5eb8.
[55] Stamati O, Roubin E, Andò E, Malecot Y. Tensile failure of micro-concrete: from mechanical tests to fe meso-model with the help of x-ray tomography. Meccanica 2019;54:707–22.
[56] Y. Sun, Finite element modeling of the cyclic behavior of concrete: mesoscopic approaches, Ph.D. thesis, Université de Lille, Bâtiment ESPRIT, Cité Scientifique,

Villeneuve-d'Ascq, 2019. URL: http://ori-nuxeo.univ-lille1.fr/nuxeo/site/esupversions/80e97ee9-810c-44e1-8fc5-a9dc72d7231e.

[57] Benkemoun N, Gelet R, Roubin E, Colliat J-B. Poroelastic two-phase material modeling: theoretical formulation and embedded finite element method implementation. Int. J. Numer. Anal. Meth. Geomech. 2015;39:1255–75.

[58] Linder C, Rosato D, Miehe C. New finite elements with embedded strong discontinuities for the modeling of failure in electromechanical coupled solids. Comput Methods Appl Mech Eng 2011;200:141–61.

[59] Stamati O, Roubin E, Andò E, Malecot Y. Phase segmentation of concrete x-ray tomographic images at meso-scale: Validation with neutron tomography. Cem Concr Compos 2018;88:8–16.

[60] Stanic A, Brank B, Brancherie D. Fracture of quasi-brittle solids by continuum and discrete-crack damage models and embedded discontinuity formulation. Eng Fract Mech 2020;227:106924.

[61] Crack propagation simulation without crack tracking algorithm: Embedded discontinuity formulation with incompatible modes. Comput Methods Applied Mech Eng 2021;386 114090.

[62] Ibrahimbegovic A. Nonlinear Solid Mechanics: Theoretical Formulations and Finite Element Solution Methods. Solid Mechanics and Its Applications. Netherlands: Springer; 2009. URL: https://books.google.fr/books?id=Py-CKiWuiY4C.

[63] Hauseux P, Roubin E, Colliat J-B. The embedded finite element method (e-fem) for multicracking of quasi-brittle materials. In: Shojaei AK, Shao J, editors. Porous Rock Fracture Mechanics. Woodhead Publishing; 2017. p. 177–96. https://doi.org/10.1016/B978-0-08-100781-5.00008-7.

[64] Benkemoun N, Roubin E, Colliat J-B. Fe design for the numerical modelling of failure induced by differential straining in meso-scale concrete: Algorithmic implementation based on operator split method. Finite Elem Anal Des 2017;137.

[65] Ortega Laborin A, Roubin E, Malecot Y, Daudeville L. General consistency of strong discontinuity kinematics in embedded finite element method (e-fem) formulations. Materials 2021;14.

[66] Karavelic E, Nikolic M, Ibrahimbegovic A, Kurtovic A. Concrete meso-scale model with full set of 3d failure modes with random distribution of aggregate and cement phase. part i: Formulation and numerical implementation. Comput Methods Appl Mech Eng 2019;344:1051–72.

[67] Ibrahimbegovic A, Rukavina I, Suljevic S. Multiscale model with embedded discontinuity discrete approximation capable of representing full set of 3d failure modes for heterogeneous materials with no scale separation. Int J Multiscale Comput Eng 2022;20:1–32.

[68] Taylor RL. FEAP - finite element analysis program; 2014. URL: http://www.ce.berkeley/feap.

[69] Stamati O, Andò E, Roubin E, Cailletaud R, Wiebicke M, Pinzon G, Couture C, Hurley RC, Caulk R, Caillerie D, Matsushima T, Bésuelle P, Bertoni F, Arnaud T, Ortega Laborin A, Rorato R, Sun Y, Tengattini A, Okubadejo O, Colliat J-B, Saadatfar M, Garcia FE, Papazoglou C, Vego I, Brisard S, Dijkstra J, Birmpilis G. 'spam': Software for practical analysis of materials. J Open Source Software 2020;5:2286.

[70] Geuzaine C, Remacle J-F. Gmsh: a three-dimensional finite element mesh generator with built-in pre- and post-processing facilities. Int J Numer Meth Eng 2009;79:1309–31.